Available online at www.sciencedirect.com

ScienceDirect

Geochimica et Cosmochimica Acta 261 (2019) 145–170

Geochimica et Cosmochimica Acta

www.elsevier.com/locate/gca

Elemental and isotopic variability in solar system materials by mixing and processing of primordial disk reservoirs

Christoph Burkhardt [a,b,*], Nicolas Dauphas [b], Ulrik Hans [c], Bernard Bourdon [d], Thorsten Kleine [a]

[a] Institut für Planetologie, University of Münster, Wilhelm Klemm-Straße 10, D-48149 Münster, Germany
[b] Origins Laboratory, Department of the Geophysical Sciences and Enrico Fermi Institute, The University of Chicago, 5734 South Ellis Avenue, Chicago, IL 60637, USA
[c] EMPA, Laboratory for Advanced Materials and Surfaces, Überlandstrasse 129, CH-8600 Dübendorf, Switzerland
[d] Laboratoire de Géologie de Lyon, ENS Lyon, CNRS and Université Claude Bernard Lyon 1, 69364 Lyon cedex 07, France

Received 28 December 2018; accepted in revised form 1 July 2019; Available online 9 July 2019

Abstract

Isotope anomalies among planetary bodies provide key constraints on planetary genetics and the solar system's dynamical evolution. However, to unlock the full potential of these anomalies for constraining the processing, mixing, and transport of material in the disk it is essential to identify the main components responsible for producing planetary-scale isotope variations, and to investigate how they relate to the isotopic heterogeneity inherited from the solar system's parental molecular cloud. To address these issues we measured the Ti and Sr isotopic compositions of Ca,Al-rich inclusions (CAIs) from the Allende CV3 chondrite, as well as acid leachates and an insoluble residue from the Murchison CM2 chondrite, and combine these results with literature data for presolar grains, hibonites, chondrules, and bulk meteorites. Our analysis reveals that the internal mineral-scale nebular isotopic heterogeneity as sampled by leachates and presolar grains is largely decoupled from the planetary-scale isotope anomalies as sampled by bulk meteorites. We show that variable admixing of CAI-like refractory material to an average inner solar nebula component can explain the planetary-scale Ti and Sr isotope anomalies and the elemental and isotopic difference between non-carbonaceous (NC) and carbonaceous (CC) nebular reservoirs for these elements.

Combining isotope anomaly data for a large number of elements (Ti, Sr, Ca, Cr, Ni, Zr, Mo, Ru, Ba, Nd, Sm, Hf, W, and Os) reveals that the offset of the CC from the NC reservoir towards the composition of CAIs is a general trend and not limited to refractory elements. This implies that the CC reservoir is the product of mixing between NC material and a reservoir (called IC for Inclusion-like Chondritic component) whose isotopic composition is similar to that of CAIs, but whose chemical composition is similar to bulk chondrites. In our preferred model, the distinct isotopic compositions of these two nebular reservoirs reflect an inherited heterogeneity of the solar system's parental molecular cloud core, which therefore has never been fully homogenized during collapse. Planetary-scale isotopic anomalies are thus caused by variable mixing of isotopically distinct primordial disk reservoirs, the selective processing of these reservoirs in different nebular environments, and the heterogeneous distribution of the thereby forming nebular products.

Keywords: Nucleosynthesis; Meteorites; CAIs; Ti isotopes; Sr isotopes; Early solar system

* Corresponding author at: Institut für Planetologie, University of Münster, Wilhelm Klemm-Straße 10, D-48149 Münster, Germany. Fax: +49 251 83 36301.
E-mail address: burkhardt@uni-muenster.de (C. Burkhardt).

https://doi.org/10.1016/j.gca.2019.07.003
0016-7037/

1. INTRODUCTION

The solar system formed ~4.567 Ga ago by the gravitational collapse of a cold and dense molecular cloud core whose chemical and isotopic composition reflects ~9 Ga of galactic chemical evolution (*e.g.*, Dauphas, 2005). Insights into the nature of the materials present at solar system formation—and the processes that acted on them—can be gained by analyzing chondritic meteorites, which derive from asteroids that have not undergone melting and chemical differentiation, and as such have preserved a record of the processes that affected solid material in the circumstellar disk prior to their incorporation into planetary bodies.

The identification of extreme mass-independent isotopic anomalies in minerals from the matrices of chondrites reveals that the solar system's parental molecular cloud contained dust particles with distinctive nucleosynthetic signatures inherited from previous generations of stars, and that some of this dust survived processing in the solar system (*e.g.*, Zinner, 2014). However, these presolar grains make up at most 0.2‰ of a primitive chondrite. All other chondrite components show signs of reprocessing in the interstellar medium (*e.g.*, aggregate formation and amorphization by cosmic rays), high-temperature processing in the solar accretion disk (*e.g.*, evaporation, condensation, and melting), and aqueous alteration and heating on meteorite parent bodies. All these processes likely contributed to the homogenization of primary nucleosynthetic signatures. Nevertheless, small but resolvable isotope anomalies are present in most solar system materials (for a recent summary see Dauphas and Schauble, 2016).

Different chondrite classes exhibit significant textural, mineralogical, and chemical variability (*e.g.*, in abundance of volatile elements or CAIs, in the ratio of chondrules to matrix, or in the bulk oxygen contents), attesting to the variable physico-chemical conditions that prevailed in the early solar system (Scott and Krot, 2014). These variable conditions provide evidence for selective processing and fractionation of molecular cloud material in different regions of the solar nebula and at different times. Therefore, it is no surprise that resolvable nucleosynthetic isotope variations are present among bulk meteorites. Although the resulting isotopic variations are small (*i.e.*, in the parts-per-ten-thousand to parts-per-million range; compared to orders-of-magnitude variations in presolar grains of circumstellar origin), they provide a means of testing models for the dynamical evolution of the (proto-)planetary disk and the accretion history of planets. For example, nucleosynthetic isotopic anomalies (*i*) affect radioisotope systems used to establish the chronology of the solar system (Burkhardt et al., 2012a, 2016; Hans et al., 2013; Render et al., 2017; Boyet et al., 2018); (*ii*) allow determining the building material of the Earth (*e.g.*, Burkhardt et al., 2011, 2016; Warren, 2011) and how this may have changed over time (Dauphas, 2017; Schiller et al., 2018; Budde et al., 2019); and (*iii*) drive the development of new types of giant impact models for the origin of the Moon (*e.g.*, Pahlevan and Stevenson, 2007; Lock et al., 2018).

Finally, in the past few years it has been realized that nucleosynthetic isotope anomalies allow distinguishing between material originating from at least two fundamentally different nebular source regions, which have been termed the non-carbonaceous (NC) and carbonaceous (CC) reservoirs (Warren, 2011; Budde et al., 2016). These two reservoirs have been isolated from each other for several million years, most likely due to the early formation of Jupiter in between them (Warren, 2011; Budde et al., 2016; Van Kooten et al., 2016; Kruijer et al., 2017). Although it has been long known that most carbonaceous chondrites are isotopically distinct from other meteoritic and planetary materials (*e.g.*, Clayton et al., 1976; Niemeyer, 1988; Leya et al., 2008), and it has been noted that in multi-elemental isotope space meteorites define distinct clusters (Trinquier et al., 2007, 2009; Regelous et al., 2008), it was Warren (2011) who pointed out the fundamental 'gap' between the two clusters and who introduced the terms non-carbonaceous (NC) and carbonaceous meteorites (CC) as taxonomic super-groups. Subsequent work demonstrated that the NC-CC dichotomy extends to a wide range of elements (*e.g.*, Mo, Ni, Ru, W), and also holds for differentiated meteorites, which derive from bodies that accreted within the first ~1 Ma of the solar system. As such, the NC-CC dichotomy is a fundamental and ubiquitous characteristic of the early solar system that has been established very early.

These examples highlight how planetary-scale nucleosynthetic anomalies provide key constraints on fundamental aspects of disk dynamics and planet formation. However, a clear understanding of how processing, mixing, and transport of dust during the early evolution of the solar accretion disk gave rise to large-scale isotopic anomalies is still lacking. Two endmember scenarios have been proposed to account for the isotopic heterogeneity observed at the bulk meteorite scale (Fig. 1). Either the

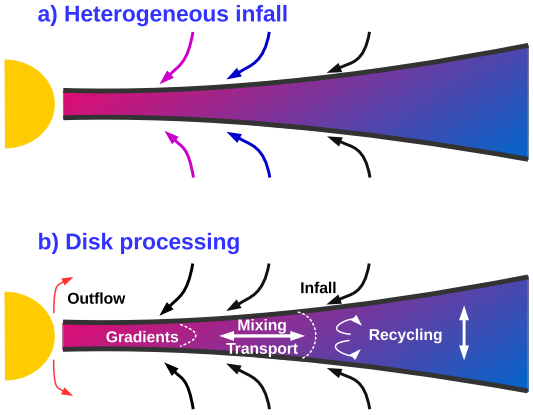

Fig. 1. Nonexclusive scenarios proposed to account for the isotopic heterogeneity at the bulk meteorite scale. Planetary-scale isotope anomalies are either (a) a primordial feature of the solar nebula inherited from heterogeneities in the infalling presolar molecular cloud materials, or (b) they are caused by fractionation processes within the solar nebula, such as separation of dust grains of different types and sizes, or the selective destruction of thermally labile presolar components.

bulk anomalies are a primordial feature of the solar nebula inherited from heterogeneities in the infalling molecular cloud material, *e.g.*, due to a late injection of freshly synthesized matter (Clayton, 1982; Dauphas et al., 2002, 2004; Bizzarro et al., 2007), or they are caused by fractionation processes of an initially homogeneous cloud, either during infall (Van Kooten et al., 2016), or within the solar nebula itself (Dauphas et al., 2004, 2010; Regelous et al., 2008; Trinquier et al., 2009; Burkhardt et al., 2012b; Paton et al., 2013; Akram et al., 2015; Schiller et al., 2015; Pignatale et al., 2017; Poole et al., 2017). Such fractionation processes may involve the separation of dust grains of different types and sizes, or the selective destruction of thermally labile presolar components. For example, transport of dust in the disk, settling of dust to the midplane, or turbulences in the disk may have fractionated small presolar grains from larger isotopically more normal dust, leading to the formation of isotopically distinct disk regions (*e.g.*, Dauphas et al., 2010). Likewise, thermal processing of dust along gradients in the disk will affect refractory presolar phases differently than thermally more labile phases, and may also have produced isotopically distinct disk reservoirs (*e.g.*, Burkhardt et al., 2012b). Although these scenarios and processes can account for the presence of ε-level isotopic anomalies in bulk meteorites and planets, until now they have not been linked to specific nebular conditions. As such, a holistic and quantitative model for the distribution of nucleosynthetic anomalies in planetary materials is lacking. This is because for many elements neither the presolar carriers of the nucleosynthetic anomalies, nor their behavior in different nebular settings are known. Furthermore, for many elements the individual presolar carriers may relate to the generation of bulk anomalies only in an indirect way, through the redistribution of materials (such as CAIs and chondrules) formed by dust processing in the solar nebula.

Here we combine new concentration and Ti and Sr isotope data for acid leachates and an insoluble residue from the Murchison CM2 carbonaceous chondrite, as well as for Allende CAIs, with existing isotope anomaly data for nebular and planetary materials to improve our understanding of the generation of planetary-scale isotopic anomalies for Ti and Sr. By comparing the results with data for other elements, we develop a quantitative model for the origin of planetary-scale anomalies and the causes for the offset between the non-carbonaceous (NC) and carbonaceous (CC) nebular reservoirs in the context of the evolution of the early solar system.

2. SAMPLES AND METHODS

The leachate samples investigated here for their multi-elemental concentration and Ti and Sr isotopic composition are aliquots of a sequential dissolution of ~16.5 g whole-rock powder of the carbonaceous chondrite Murchison, which was performed at the University of Chicago using the following sequence:

L1:	9 M HAc (acetic acid), 1 day, 20 °C;
L2:	4.7 M HNO_3, 5 days, 20 °C;
L3:	5.5 M HCl, 1 day, 75 °C;
L4:	13 M HF – 3 M HCl, 1 day, 75 °C;
L5:	13 M HF – 6 M HCl, 3 days, 150 °C;
L6:	Insoluble residue.

The aliquot of the insoluble residue (L6) was fused by a CO_2 laser under a reducing atmosphere before digestion in HNO_3–HF–$HClO_4$ (see Burkhardt et al., 2012b). Molybdenum and W isotopic compositions on the same aliquots have been reported in Burkhardt et al. (2012a, b), and Ca, Cr, Ru, and Os isotope compositions obtained on different aliquots of the sequential digestion are given in Chen et al. (2011), Papanastassiou et al. (2010), Fischer-Gödde et al. (2014), and Reisberg et al. (2009), respectively.

The five Allende CAIs analyzed here for their multi-elemental concentration and Ti and Sr isotopic composition have also been previously investigated for Mo and W isotope systematics (Burkhardt et al., 2008, 2011), and for two of them (A-ZH-2, A-ZH-4) Sr isotope data were reported in Hans et al. (2013). The CAIs A-ZH-1 to A-ZH-4 are typical large coarse-grained type B igneous inclusions consisting mainly of melilite and fassaite, while CAI A-ZH-5 has a more fine-grained appearance with voids and alteration features (Burkhardt et al., 2008).

After digestion and treatment with aqua regia, all samples were dried down and redissolved in 6 M HCl–0.01 M HF. At this point ~0.4–5% aliquots were taken for concentration measurements. The remaining solutions were processed through ion exchange chromatography to separate Sr, Ti (this study), and Mo and W (Burkhardt et al., 2008, 2012a,b).

Strontium, along with the main matrix elements, was separated from the high field strength elements, Mo, and W on a primary cation exchange column (14 mL AG50W-X8 200–400 mesh) with 1 M HCl–0.1 M HF (Patchett and Tatsumoto, 1980). Strontium and the matrix elements were washed off this column with 6 M HCl. After drying down, Sr was separated from the matrix and Rb in 2.5 M HCl on an ion exchange column filled with 3.6 mL BioRad AG50W-X8 (200–400 mesh). After evaporation, the Sr cuts were re-dissolved in 3 M HNO_3 and further purified using a 200 µL Eichrom Sr resin column (Hans et al., 2013). Rubidium was washed off this column in 3 M HNO_3 together with the matrix elements, while Sr was eluted with 0.05 M HNO_3. After conversion into chloride form the Sr was then ready for measurement by TIMS. The total procedural blank for the Sr separation was ~14 pg, which is negligible given the high Sr contents of the samples.

The elution cut containing HFSE, Mo, and W was dried down and re-dissolved in 1 M HF (leachates) or 1 M HCl–0.1 M HF (CAIs) and loaded on columns filled with AG1-X8 (100–200 mesh) anion exchange resin. For the leachate samples the remaining matrix was washed off these columns

in 1 M HF, followed by elution of Ti (+Zr, Hf) in 6 M HCl–0.06 M HF, before W was eluted in 6 M HCl–1 M HF, and finally Mo in 3 M HNO_3. The matrix of the CAI samples was washed off in 0.5 M HCl–0.5 M HF, Ti (+Zr, Hf) in 3.6 M HAc–2% H_2O_2, W in 6 M HCl–1 M HF, and Mo in 6 M HNO_3–0.2 M HF, respectively (Burkhardt et al., 2008, 2012b). Titanium was further purified in Chicago following the methods laid out by Zhang et al. (2011). After drying down, the cuts were taken up in aqua regia, dried and re-dissolved in 12 M HNO_3 (+traces of H_3BO_3) and loaded on columns prepacked with 2 mL Eichrom DGA resin. After rinsing off the matrix in 12 M HNO_3, Ti was eluted with a mixture of 12 M HNO_3–1 wt.% H_2O_2 while Zr and Hf stayed on the column. Titanium cuts were dried with concentrated HF and finally loaded on pre-cleaned anion exchange columns (AG1-X8, 0.8 mL, 200–400 mesh) in 4 M HF. After washing off the matrix and V, Ti was eluted with 9 M HCl–0.01 M HF, and, after conversion to 0.3 M HNO_3–0.0014 M HF solutions, was ready for measurement by MC-ICPMS.

The Ti isotope measurements were performed using the ThermoFisher Scientific Neptune MC-ICP-MS at the Origins Lab in Chicago in high resolution mode (Zhang et al., 2011). Solutions containing about 275 ppb Ti were introduced through a Cetac Aridus II desolvating system, resulting in a $\sim 4.5 \times 10^{-10}$ A ion beam on ^{48}Ti. Measurements consisted of a two-line data acquisition scheme. The first line measured all Ti isotopes as well as a Ca interference monitor on mass 44, and the second line measured masses 49 and 50, as well as V and Cr interference monitors on masses 51 and 53. Measurements were performed on the peak shoulder to resolve polyatomic isobaric interferences of $^{22}Ne^{22}Ne^{+}$ on mass 44, $^{36}Ar^{14}N^{+}$ on mass 50 and $^{40}Ar^{13}C^{+}$ on mass 53. Each measurement consisted of a 30 s baseline (deflected beam) followed by 20 isotope ratio measurements of 16 s each. Interference corrections were small (maximum Ca correction was -0.47 $\varepsilon^{48}Ti$) and well within the previously defined correctable range (Zhang et al., 2011), or negligible (V, Cr, *i.e.* < 0.05 $\varepsilon^{50}Ti$). The Ti isotope results are given as $\varepsilon^{i}Ti$ relative to bracketing measurements of the Origins Lab OL-Ti standard ($\varepsilon^{i}Ti = [(^{i}Ti/^{47}Ti)_{sample}/(^{i}Ti/^{47}Ti)_{OL\text{-}Ti} - 1] \times 10^{4}$; with i = 46, 48, 50). Instrumental mass bias was corrected using $^{49}Ti/^{47}Ti = 0.749766$ as normalizing ratio with the exponential law. The external reproducibility (2 s.d.) of the standard during the analytical session was ± 0.22 $\varepsilon^{46}Ti$, ± 0.12 $\varepsilon^{48}Ti$, and ± 0.38 $\varepsilon^{50}Ti$. The accuracy and reproducibility of the Ti isotope measurements was assessed by analyses of the terrestrial rock standard BHVO-2 and the CV3 chondrite Allende, both of which agree with previously published results.

Strontium isotope measurements were performed using the ThermoFisher Scientific Triton TIMS at ETH Zurich. For each measurement about 500 ng of Sr was loaded on a previously out-gassed (4 A for 2 h with a 30 min peak at 4.5 A) Re single filament. Approximately 1 μL of sample in 6 M HCl was mixed with 1 μL of $TaCl_5$ activator containing phosphoric acid solution prior to loading. Two fine strips of Parafilm were used to prevent spreading of the sample solution. The samples were then loaded with a Hamilton syringe and dried down at 0.6 A. The Parafilm strips were burnt off at 1.2 A and the filament then glowed briefly to dull red at 2 A. Rubidium interferences were monitored by measuring ^{85}Rb. Some samples contained minor Rb, but this was burnt off the filament prior to the Sr isotopic measurements, such that Rb interference corrections were negligible for all samples. Depending on sample size, Sr isotopes were measured at ^{88}Sr intensities between 5×10^{-11} A and 2×10^{-10} A for 8–10 h and consisted of 800 cycles. Baselines were measured for 30 seconds prior to each block of 20 cycles.

The $^{84}Sr/^{86}Sr$ measurements were performed by either a one-line static acquisition scheme or a two-line acquisition scheme. In the latter case, ^{84}Sr was collected in the cups L1 and L3, with all other Sr isotopes collected accordingly in each magnet setting. Integration times were 8 s for each line with a 3 s idle time between mass jumps. The $^{84}Sr/^{86}Sr$ ratios acquired in each line were corrected for instrumental mass fractionation with the exponential law using the $^{86}Sr/^{88}Sr$ ratio acquired in the same line and assuming $^{86}Sr/^{88}Sr = 0.1194$. A 'multi-static' $^{84}Sr/^{86}Sr$ ratio can then be obtained by averaging the two static $^{84}Sr/^{86}Sr$ ratios acquired in the two lines. A dynamic $^{84}Sr/^{86}Sr$ ratio is obtained by correcting the $^{84}Sr/^{86}Sr$ ratio measured in the first line for mass fractionation using the $^{86}Sr/^{88}Sr$ obtained in the second line. With this latter procedure, potential biases in cup efficiencies and gain factors of the amplifiers effectively cancel out (Hans et al., 2013) and yield more reliable results compared with static measurements. Repeated measurement of the NBS 987 Sr standard over the course of this study yielded ratios of $^{84}Sr/^{86}Sr = 0.0564943 \pm 0.0000016$ for the dynamic measurements (2 s.d.) and $^{84}Sr/^{86}Sr = 0.0564925 \pm 0.0000025$ for the multi-static measurements (2 s.d.).

Concentration measurements on digestion aliquots were performed on a ThermoFisher Scientific Element II quadrupole ICP-MS at the Institute für Planetologie at the University of Münster for the leachate samples, and an Elan quadrupole ICP-MS at ETH Zürich for the CAIs. The samples were introduced into the plasma without prior chemical separation and concentrations were calculated by comparing the count rates of the samples to multi-element standard solutions. The uncertainties on the concentrations are estimated for each element individually by comparing the concentrations of BCR-2, BHVO-2, JA-2, DTS-2a and Allende standard solutions measured alongside the unknowns at similar or lower intensity relative to literature reference values (Jarosewich et al., 1987; Stracke et al., 2012; Jochum et al., 2015).

3. RESULTS

3.1. Leachate concentration data

The concentrations of the Murchison leachates are given in Table 1 and are shown in Figs. 2 and 3 for selected elements. The leachate concentrations were calculated by dividing the total quantity of the element in the leachates by the total mass of the Murchison sample (~16.5 g), such that the sum of the concentrations in the individual lea-

Table 1
Element concentration data of Murchison leachates.

Analyte	Unit	L1	L2	L3	L4	L5	L6	Total	σ %
Li	ng/g	320	383	103	4.3	1.3	13	824	5
Na	µg/g	3110	90.6	48.6	6.36	4.26	3.53	3263	3
Mg	µg/g	31,874	53,182	10,217	3280	142	10,822	109,518	8
Al	µg/g	2554	4566	527	76.22	39.6	715.96	8479	3
K	µg/g	291	47.9	2.56	2.50	0.81	1.30	346	6
Ca	µg/g	6586	991	2259	747	55.0	612	11,250	5
Sc	µg/g	1.9	2.9	1.6	n.d.	n.d.	1.2	7.7	40
Ti	µg/g	22.7	143	210	207	9.67	1.99	595	5
V	µg/g	10.46	26.78	10.94	6.63	3.53	5.38	63.7	11
Cr	µg/g	645	833	300	424	244	158	2604	10
Mn	µg/g	760	417	151	159	14.4	9.3	1511	8
Fe	µg/g	120,232	60,488	6843	607	144	227	188,541	10
Co	µg/g	182	289	7.1	0.60	0.21	0.49	479	12
Ni	µg/g	4403	4763	117	6.4	2.6	28.9	9321	11
Cu	µg/g	0.22	90.9	2.61	0.47	0.13	0.32	94.6	12
Zn	µg/g	129	38.7	2.34	0.86	0.41	0.10	172	15
Ga	ng/g	624	5794	199	63	77	1.2	6759	25
Rb	ng/g	885	653	20.0	1.82	0.66	0.88	1561	2
Sr	ng/g	8203	976	389	54.9	7.53	75.1	9705	6
Y	ng/g	722	229	548	7.86	3.30	288	1798	7
Zr	ng/g	797	836	253	1013	395	1108	4403	4
Nb	ng/g	1.3	2.1	20	279	46	20	369	30
Mo	*ng/g*	*49.0*	*784.4*	*213.3*	*74.6*	*8.3*	*24.1*	*1154*	*0.1*
Ru	ng/g	194	167	37.0	5.4	5.1	8.8	417	8
Rh	ng/g	30.7	70.2	15.9	1.99	0.11	11.1	130	10
Pd	ng/g	46	41	180	11	n.d.	190	468	30
Ag	ng/g	4.0	48.6	51.1	8.8	2.1	3.6	118	80
Cd	ng/g	306	103	7.46	3.90	1.21	1.71	423	80
In	ng/g	42.10	7.47	1.32	0.35	0.19	0.02	51.4	18
Ba	ng/g	908	631	37.3	2.75	0.75	19.9	1600	2
La	ng/g	206	42.7	53.9	0.91	0.35	17.0	321	5
Ce	ng/g	447	107	162	2.23	1.08	49.7	769	3
Pr	ng/g	62.3	15.2	27.8	0.33	0.17	8.6	114	3
Nd	ng/g	301	71.8	160	1.94	1.25	49.8	586	5
Sm	ng/g	95.1	23.8	55.5	1.00	0.46	21.1	197	6
Eu	ng/g	58.2	9.30	4.53	0.09	0.08	1.19	73.4	7
Gd	ng/g	114	34.3	81.2	0.94	0.69	34.3	266	16
Tb	ng/g	18.52	6.33	14.72	0.18	0.15	6.42	46.3	3
Dy	ng/g	129	42.9	100	1.57	1.06	47.0	321	4
Ho	ng/g	26.9	9.38	21.42	0.36	0.20	10.9	69.1	6
Er	ng/g	83.9	28.1	62.3	1.36	0.57	32.8	209	7
Tm	ng/g	12.9	3.95	8.83	0.12	0.06	4.77	30.7	6
Yb	ng/g	90.5	26.1	54.9	0.55	0.31	28.9	201	9
Lu	ng/g	12.3	4.2	8.1	0.17	0.04	5.35	30.2	5
Hf	*ng/g*	*14.49*	*30.70*	*10.48*	*41.22*	*8.47*	*23.73*	*129*	*0.2*
Ta	ng/g	0.14	n.d.	0.19	14.18	2.75	0.52	18	24
W	*ng/g*	*7.83*	*20.85*	*27.42*	*59.43*	*3.00*	*4.50*	*123.0*	*0.8*
Re	*ng/g*	*16.0*	*22.0*	*2.3*	*0.50*	*0.30*	*6.0*	*46*	*15*
Os	*ng/g*	*117*	*265*	*69*	*12*	*20*	*63*	*547*	*3*
Ir	ng/g	144	168	59	10.3	2.8	77	461	30
Pt	*ng/g*	*93*	*243*	*200*	*21*	*5*	*339*	*900*	*1.9*
Tl	ng/g	0.30	58.4	1.07	0.23	0.23	0.00	60	14
Pb	ng/g	97	1087	24	5.3	1.9	0.5	1216	50
Bi	ng/g	4.5	39	4.8	0.36	0.09	0.07	49	22
Th	ng/g	18	15	7.5	0.05	0.07	2.7	43	20
U	ng/g	5.8	1.3	1.6	0.07	0.10	0.60	9.5	28

Concentrations in the leachates were calculated by dividing the quantity of the element in the leachate by the total mass of the Murchison sample. Uncertainty is estimated by average deviation of concentrations of BCR-2, BHVO-2, JA-2, DTS-2a, and Allende solutions (measured at similar or lower intensity along with the leachates) from literature reference values (Jarosewich et al., 1987; Stracke et al., 2012; Jochum et al., 2015). Values in italic were obtained by isotope dilution in Burkhardt et al. (2012a,b) (Mo, Hf, W) and Reisberg et al. (2009) (Re, Os, Pt).

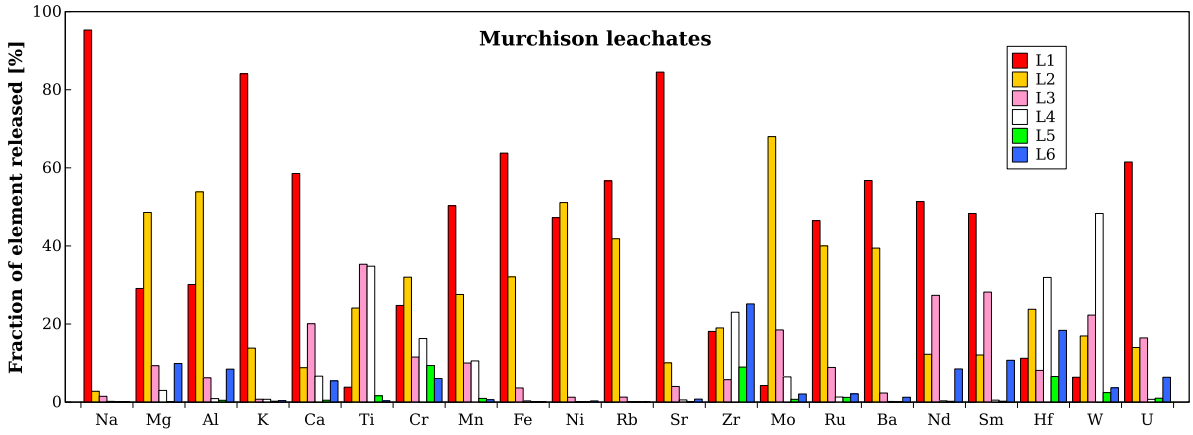

Fig. 2. Release patterns of selected elements obtained by a six-step sequential digestion of a powdered sample of the Murchison (CM2) meteorite.

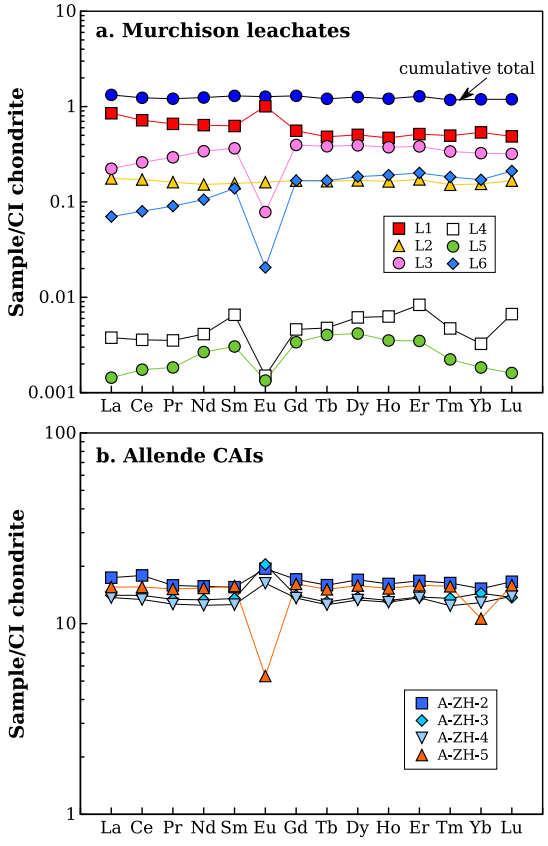

Fig. 3. Chondrite-normalized REE abundance patterns. (a) Murchison leachates exhibit a large range in concentrations and subtle differences in the shape of the patterns, however, the cumulative total of all leachates and the residue has a flat REE pattern and an enrichment (~1.25 × CI) consistent with bulk CM literature data. (b) Investigated Allende CAIs exhibit about flat REE patterns with ~15 × CI enrichment. CAI A-ZH-5 has negative volatility controlled excursions in Eu and Yb (group III pattern).

chates should add up to the bulk Murchison concentration. Except for elements that have been partly lost by evaporation during sample preparation (*e.g.,* Ru), the agreement with average CM chondrite data from the literature is very good, *e.g.*, for Ti and Sr with 595 ± 9 and 9.7 ± 0.4 μg/g here *vs.* 580 and 10.1 μg/g in Wasson and Kallemeyn (1988), respectively. This suggests that our measurements are accurate and that all components of Murchison were digested in the leaching procedure. Leach step 1 (9 M acetic acid at room temperature) contains 50% of the total mass of the elements analyzed. Nearly all of the highly soluble lithophile elements Na (95%), K (84%), Sr (85%), and the majority (>50%) of In, Ca, Mn, Fe, Zn, Rb, Cd, Ba, LREE, and U present in Murchison are dissolved in the acetic acid leachate. This acid attacked halites, carbonates, phosphates, soluble organic matter, as well as some metal and silicates. The CI chondrite normalized REE abundance reveals subtle enrichments of LREE vs. HREEs and a positive Eu anomaly in the acetic acid leachate (Fig. 3a). Leach step 2 (4.7 M HNO_3 at room temperature) contains 37% of the total mass of the analyzed elements. Most abundant is Fe (32% of total Fe), followed by Mg (49%), Ga (86%), Ni (51%) and Al (54%). This leachate contains the majority of all Tl (97%), Cu (96%), Pb (89%), Ga (86%), Bi (80%), Mo (68%) Co (60%), Rh (54%), Ni (51%), and major fractions of V, Ag, Ru, Re, and Os, and thus indicates digestion of metals and sulfides along with some oxides and silicates. The REE abundances are about a factor of 3–5 times lower than in the acetic acid and no LREE enrichment or Eu anomaly is visible (Fig. 3a). Leachate 3 (5.5 M HCl at 75 °C) contains 6.4% of the total mass of the analyzed elements. Dominant are Mg (9.3% of total Mg), Fe (1.3%), Ca (20%) and Ti (35%). The REE are more abundant than in leach step 2, but lower than in leach step 1. They display a deficit in LREE relative to HREE and a negative Eu anomaly. Leach step 4 (13 M HF–3 M HCl at 75 °C) dissolved 1.9% of the total mass of the analyzed elements. Most abundant is Mg (3% of total Mg), followed by Ca (6.6%) and Fe (0.3%). Due to HF, the abundances of

HFSEs (Ti 35%, Zr 23%, Nb 76%, Hf 32%, Ta 80%, W 48%) in this leachate are high, while the REEs are almost two orders of magnitude lower than in the leachate 3. Leachate 5 (13 M HF–6 M HCl at 150 °C) contains the least amount of material and dissolved only about 0.34% of the total mass of the elements analyzed. Only V, Cr, Zr, Nb, Hf and Ta are present in significant concentrations (>5% of total); while the REE abundances are down to ~0.1% of the chondritic values. The insoluble residue left after leach step 5 represents about 7.8% by weight of the Murchison starting powder and is strongly enriched in insoluble organic matter and highly refractory phases such as oxides and carbides. Fusion by laser under reducing conditions volatilized the organic (and other potentially remaining volatile) compounds and left an ultra-refractory residue of ~2.5% of the initial Murchison starting material. The residue is dominated by Mg (10% of total Mg) and Al (8%) and contains significant amounts of Pd (41%), Pt (38%), Zr (25%), Sc, Y, Re, Os, Ir, REE, and Hf (8–18%). Given the similar geo/cosmochemical behavior of Zr, Hf, and Ti the fraction of the latter in the refractory residue (0.3%) is somewhat lower than expected. This may indicate the formation of insoluble Ti-oxides during chemical processing of this sample, possibly through oxidation of $TiCl_4$ during dry-downs with $HClO_4$. The REE pattern of the residue shows a LREE depletion and a negative Eu anomaly, similar to the pattern of leachate 3. Integrating the REE concentrations of leachate 1 to 6 gives a flat REE pattern for the cumulative total with an enrichment of ~1.2 relative to CI (Fig. 3a), consistent with average bulk CM literature values (Wasson and Kallemeyn, 1988).

3.2. CAI concentration data

The concentration data of the Allende CAIs are given in Table 2 and CI chondrite normalized REE patterns are shown in Fig. 3b. As expected for refractory inclusions, all CAIs are strongly enriched in refractory elements, with enrichments ranging from 5 × CI for U in A-ZH-2 to 25 × CI for Sr in A-ZH-3. The average enrichment factors for CAIs A-ZH-1 to −5 relative to CI as based on Y, Zr, REE (except Eu), and Th concentrations are 15.0, 16.6 ± 1.1, 13.9 ± 0.6, 13.5 ± 1.0, 15.5 ± 1.6, respectively. The enrichment factors of Mo, W, and U are significantly lower than those of the other refractory elements in all CAIs. While for U this may relate to its relative volatility relative to other refractory elements, the relative depletions of Mo and W indicate volatility-controlled loss in oxidizing conditions (Fegley and Palme, 1985). In addition, the 2+ elements Sr, Ba, and Eu (melilite compatible) are all depleted in CAI A-ZH-5. The REE patterns of the CAIs are flat, except for a positive Eu anomaly in the type B CAIs A-ZH-2 to −4 (group I pattern; Mason and Martin, 1977) and a negative Eu and Yb anomaly for A-ZH-5 (group III pattern). Europium and Yb are the most volatile REEs during condensation from a gas of solar composition (Boynton, 1975; Davis and Grossman, 1979). Furthermore, CAI A-ZH-5 is enriched in volatile Rb (1.7 × CI), but not in Pb. The presence of alkalis is also consistent with extensive alteration previously documented in fine grained CAIs. Taken together, this indicates different nebular conditions during formation or processing of A-ZH-5 and the other CAIs in the circumsolar disk.

3.3. Leachate isotope data

The Ti and Sr isotopic data for the Murchison leachates are reported in Table 3 and are shown in Figs. 4–6. The leachates exhibit significant mass-independent internal Ti and Sr isotopic heterogeneity, ranging from -5.10 ± 0.23 ε^{50}Ti and $+0.62 \pm 0.17$ ε^{84}Sr in the first leachate to $+10.54 \pm 0.26$ ε^{50}Ti and -16.18 ± 0.47 ε^{84}Sr in the residue, respectively. For a given sample the magnitude of the Ti anomaly decreases in the order $\varepsilon^{50}Ti > \varepsilon^{46}Ti > \varepsilon^{48}Ti$. The anomalies in ε^{48}Ti and ε^{46}Ti (Fig. 6a), and ε^{48}Ti and ε^{50}Ti (Fig. 6c) are negatively correlated, the ones in ε^{50}Ti and ε^{46}Ti (Fig. 6b) are positively correlated, however neither correlation defines a straight line in ε^{i}Ti and ε^{j}Ti mixing space. These results are qualitatively consistent with Ti isotope data obtained by the sequential leaching of the Orgueil CI chondrite (Trinquier et al., 2009). The weighted average of the leachates yields anomalies of $+0.48 \pm 0.10$ ε^{46}Ti, $+0.01 \pm 0.08$ ε^{48}Ti, $+3.10 \pm 0.17$ ε^{50}Ti, and $+0.35 \pm 0.18$ ε^{84}Sr (Fig. 4), all of which are fully consistent with literature data for bulk Murchison (Trinquier et al., 2009; Moynier et al., 2012; Zhang et al., 2012; Table 3). Contrary to the individual leachates, the weighted average plots on a linear array defined by bulk planetary materials, chondrules, and CAIs in ε^{50}Ti vs. ε^{46}Ti space (Fig. 6b).

The overall trend from slightly positive to strongly negative ε^{84}Sr anomalies observed here is qualitatively comparable to the results of other sequential digestion studies of Murchison (Qin et al., 2011; Yokoyama et al., 2015). The $^{87}Sr/^{86}Sr$ of the leachates is dominated by decay from ^{87}Rb ($t_{1/2} = 49.5$ Ga) and ranges from unradiogenic 0.702120 in leachate 3 to radiogenic 0.753512 in leachate 2. For comparison, the initial $^{87}Sr/^{86}Sr$ ratio at solar system birth is estimated to be 0.69875 ± 0.000008 (Hans et al., 2013), indicating that even the least radiogenic leachate fraction contains radiogenic ^{87}Sr from ^{87}Rb-decay. The $^{87}Sr/^{86}Sr$ ratio of the individual leachates are only poorly correlated with their measured $^{87}Rb/^{86}Sr$ ratio, as indicated by the significant scatter around a 4.567 Ga chondrite reference line in a Rb-Sr isochron diagram (Fig. 5a). This behavior has been observed in other leachate studies as well (Qin et al., 2011; Yokoyama et al., 2015), and suggests incongruent dissolution of Rb and Sr during the leaching procedure (note that Murchison is an observed meteorite fall and Rb/Sr mobilization by terrestrial weathering is largely irrelevant). This is supported by the observation that the weighted average $^{87}Rb/^{87}Sr$ and $^{87}Sr/^{86}Sr$ of the leachates is in the range of bulk Murchison literature values and plots well on the 4.567 Ga isochron (Fig. 5a).

3.4. CAI isotope data

The Ti and Sr isotopic data for the Allende CAIs are provided in Table 4 and are shown in Figs. 4–6. All CAIs exhibit significant and nearly uniform mass-independent non-radiogenic Ti and Sr isotopic anomalies, ranging from

Table 2
Element concentration data of Allende CAIs.

	Unit	A-ZH-1	A-ZH-2	A-ZH-3	A-ZH-4	A-ZH-5	σ %	A-ZH-1	A-ZH-2	A-ZH-3	A-ZH-4	A-ZH-5
									Relative to CI			
Mass	mg	120	180	70	200	90						
Type		B	B	B	B	A						
Group			I	I	I	III						
Rb	µg/g		*0.49*	1.95	*0.70*	3.96	9		0.21	0.84	0.30	1.71
Sr	µg/g		*186.20*	194.87	*137.10*	35.04	15		23.84	24.95	17.55	4.49
Y	µg/g		26.15	23.31	22.00	23.44	14		17.09	15.23	14.38	15.32
Zr	µg/g		60.02	51.60	52.57	61.25	9		16.58	14.25	14.52	16.92
Nb	µg/g		2.35	4.23	2.68	5.73	8		8.44	15.15	9.61	20.54
Mo	µg/g	*8.27*	*7.89*	*6.59*	*6.75*	*5.78*	*0.1*	8.50	8.11	6.77	6.94	5.94
Ba	µg/g		59.47	30.68	42.37	7.36	11		24.67	12.73	17.58	3.06
La	µg/g		4.22	3.41	3.32	3.76	10		17.43	14.09	13.70	15.55
Ce	µg/g		11.13	8.75	8.32	9.68	11		17.89	14.07	13.38	15.56
Pr	µg/g		1.50	1.27	1.20	1.44	14		15.87	13.40	12.67	15.21
Nd	µg/g		7.39	6.28	5.88	7.24	15		15.68	13.33	12.48	15.38
Sm	µg/g		2.36	2.06	1.91	2.39	14		15.53	13.55	12.59	15.76
Eu	µg/g		1.12	1.18	0.94	0.31	11		19.44	20.46	16.29	5.31
Gd	µg/g		3.49	2.87	2.79	3.31	7		17.05	14.02	13.62	16.16
Tb	µg/g		0.61	0.50	0.48	0.58	9		15.92	12.98	12.57	15.13
Dy	µg/g		4.33	3.49	3.39	4.04	9		16.98	13.70	13.30	15.84
Ho	µg/g		0.92	0.76	0.74	0.88	9		16.16	13.23	12.96	15.30
Er	µg/g		2.73	2.25	2.23	2.59	8		16.76	13.79	13.66	15.90
Tm	µg/g		0.43	0.35	0.32	0.41	9		16.33	13.57	12.42	15.69
Yb	µg/g		2.58	2.44	2.18	1.80	9		15.26	14.43	12.89	10.63
Lu	µg/g		0.42	0.35	0.35	0.40	8		16.59	13.73	13.93	15.90
Hf	µg/g	*1.60*	*2.09*	*1.57*	*1.73*	*2.05*	*0.2*	15.05	19.69	14.76	16.33	19.30
Ta	µg/g		0.21	0.20	0.20	0.23	8		14.68	14.13	13.89	16.14
W	µg/g	*1.03*	*1.22*	*1.16*	*0.96*	*1.35*	*0.8*	10.69	12.69	12.06	10.03	14.08
Pb	µg/g		0.24	0.27	0.25	0.29	8		0.09	0.10	0.10	0.11
Th	µg/g		0.46	0.42	0.42	0.46	7		14.82	13.56	13.52	14.69
U	µg/g		0.05	0.07	0.05	0.10	7		5.56	9.04	6.40	12.55

Measurements were performed on digestion aliquots containing between 0.4 to 1.4 % of the sample mass. Uncertainty is estimated by average deviation of concentrations obtained for BHVO-2 solutions (measured at similar or lower intensity as the CAIs) from literature reference values (Jochum et al., 2015). Values in italic were obtained by isotope dilution in previous studies (Burkhardt et al., 2008, 2011; Hans et al., 2013). Normalization to CI chondrites was done using data of Lodders et al. (2009).

$+9.12 \pm 0.13$ ε^{50}Ti and $+1.44 \pm 0.11$ ε^{84}Sr in A-ZH-1 to $+9.51 \pm 0.07$ ε^{50}Ti and $+1.07 \pm 0.74$ ε^{84}Sr in A-ZH-5. No resolvable differences in Ti or Sr anomalies are present between the group I (A-ZH-1 to −4) and group III (A-ZH-5) CAIs. Anomalies in ε^{46}Ti, ε^{48}Ti, and ε^{50}Ti are positively correlated, with ε^{46}Ti and ε^{48}Ti values ~5.9 and ~19 times smaller than ε^{50}Ti. Compared to previous Ti isotope studies on Allende CAIs our data show less variability, but are fully consistent with a mean anomaly peak at ~+9 ε^{50}Ti (Heydegger et al., 1982; Niemeyer and Lugmair, 1984; Niederer et al., 1985; Leya et al., 2009; Trinquier et al., 2009; Williams et al., 2016; Davis et al., 2018) (Figs. 4c, 6). In ε^{50}Ti vs. ε^{46}Ti space, CAIs, chondrules, and bulk planetary bodies plot on a common regression line (Fig. 6b), while in ε^{48}Ti vs. ε^{46}Ti and ε^{48}Ti vs. ε^{50}Ti space CAIs exhibit scatter beyond analytical uncertainty (Fig. 6a, c).

The ε^{84}Sr anomalies of the CAIs are indistinguishable within uncertainty and are well within the anomaly range reported in other studies (Moynier et al., 2012; Brennecka et al., 2013; Myojo et al., 2018). Variations in ^{87}Sr/^{86}Sr range from 0.699478 in the coarse-grained Type B CAI A-ZH-2 to 0.718868 in the more fine-grained and volatile rich A-ZH-5, and correlate with Rb/Sr as expected for a ~4.567 Ga age (Fig. 5b).

4. DISCUSSION

In the following sections we will attempt to identify the main drivers responsible for producing planetary-scale isotope variations. We investigate how planetary-scale anomalies relate to the mineral-scale isotopic heterogeneity inherited from the solar system's parental molecular cloud, and whether their formation can be accounted for solely by processes within the accretion disk itself or instead require a change in the isotopic composition of the infalling cloud material. We start by concentrating on Ti, and provide a global assessment of the relations of Ti isotopic anomalies among presolar grains, hibonites, CAIs, leachates, chondrules, matrix, and bulk planetary bodies (Section 4.1). The same is then done for Sr (Section 4.2), before we expand our analysis to multi-elemental isotope space (Section 4.3), discuss the origin of the isotope anomalies with respect to disk processing and cloud heterogeneity

Table 3
Titanium and Sr isotope data of Murchison leachates.

Sample	Procedure	Ti [μg/g] ± 2σ	Rb [ng/g] ± 2σ	Sr [ng/g] ± 2σ	$^{87}Rb/^{86}Sr \pm 2\sigma$	$\varepsilon^{46}Ti^{a} \pm 2\sigma$	$\varepsilon^{48}Ti^{a} \pm 2\sigma$	$\varepsilon^{50}Ti^{a} \pm 2\sigma$	$\varepsilon^{84}Sr^{b} \pm 2\sigma$	$^{87}Sr/^{86}Sr \pm 2\sigma$
Murchison										
L1	9 M HAc 1 day, 20 °C	22.7 ± 1	885 ± 18	8203 ± 492	0.31 ± 0.02	−0.40 ± 0.11	0.30 ± 0.06	−5.10 ± 0.23	0.62 ± 0.17	0.728748 ± 0.000002
L2	4.7 M HNO_3, 5 days, 20 °C	143 ± 7	653 ± 13	976 ± 59	1.94 ± 0.12	0.18 ± 0.16	0.07 ± 0.08	−1.04 ± 0.21	0.05 ± 0.19	0.753512 ± 0.000003
L3	5.5 M HCl, 1 day, 75 °C	210 ± 11	20.0 ± 0.4	389 ± 23	0.15 ± 0.01	0.66 ± 0.08	−0.07 ± 0.08	5.13 ± 0.17	−1.05 ± 0.29	0.702120 ± 0.000004
L4	13 M HF 3 M HCl, 1 day, 75 °C	207 ± 10	1.82 ± 0.04	54.9 ± 3	0.10 ± 0.01	0.55 ± 0.08	0.03 ± 0.08	4.46 ± 0.14	−1.64 ± 0.67	0.703798 ± 0.000008
L5	13 M HF 6 M HCl, 3 days, 150 °C	9.7 ± 0.5	0.66 ± 0.01	7.5 ± 1.0	0.25 ± 0.03	0.92 ± 0.14	−0.12 ± 0.06	9.20 ± 0.18	−2.70 ± 0.77	0.704667 ± 0.000008
L6	Insoluble residue, Laser fused	2.0 ± 0.1	0.88 ± 0.02	75.1 ± 5	0.034 ± 0.002	3.63 ± 0.10	−1.92 ± 0.10	10.54 ± 0.26	−16.18 ± 0.47	0.704959 ± 0.000006
Total (conc.) or wt. ave. (ratios)		595 ± 9	1561 ± 15	9705 ± 423	0.47 ± 0.02	0.48 ± 0.10	0.01 ± 0.08	3.10 ± 0.17	0.35 ± 0.18	0.729826 ± 0.000002
Bulk Murchison[c]		580	1700	10,100	0.49	0.54 ± 0.08	−0.05 ± 0.03	3.06 ± 0.09	0.34 ± 0.38	

[a] $\varepsilon^{i}Ti = [(^{i}Ti/^{47}Ti)_{sample}/(^{i}Ti/^{47}Ti)_{OL\text{-}Ti} - 1] \times 10^{4}$ after mass-bias correction by internal normalization to $^{49}Ti/^{47}Ti = 0.749766$ using the exponential law. Uncertainties represent Student-t 95% confidence intervals $\sigma_{0.95,n\text{-}1}/\sqrt{n}$.

[b] $\varepsilon^{i}Sr = [(^{i}Sr/^{86}Sr)_{sample}/(^{i}Sr/^{86}Sr)_{NBS\ 987} - 1] \times 10^{4}$ after mass-bias correction by internal normalization to $^{86}Sr/^{88}Sr = 0.1194$ using the exponential law. Uncertainties represent $2\sigma_{SE,mean}$.

[c] Ti, Rb, and Sr concentration from Wasson and Kallemeyn (1988); isotope data from Trinquier et al. (2009) and Moynier et al. (2012).

(Section 4.4), and finally synthesize our inferences in a global early solar system evolution model (Section 4.5).

4.1. Titanium isotope anomalies in meteoritic materials

Owing to the early discovery of Ti isotope anomalies in CAIs (Heydegger et al., 1979) and the relatively high abundance of Ti in most meteorites and chondrite components, Ti is among the elements for which isotopic anomalies have been most extensively characterized in planetary materials. However, since multiple processes and sources contribute to the Ti isotopic inventory, interpreting the meteoritic record is not straight-forward (*e.g.*, Steele and Boehnke, 2015). Measurements on hundreds of presolar grains reveal percent-level Ti isotope variations among the grains (*e.g.*, Nittler et al., 2008; Gyngard et al., 2018). The Ti isotope variability in mainstream SiC grains (the most abundant type of presolar grains, which are thought to derive from AGB stars and are characterized by large *s*-process enrichments) mainly reflect the effect of galactic chemical evolution, resulting in the increase of the secondary nuclides ^{46}Ti, ^{47}Ti, ^{49}Ti, and ^{50}Ti relative to the early-formed primary nuclide ^{48}Ti through time (Alexander and Nittler, 1999), and, more subdued, slow *n*-capture processes in the parental AGB stars (Wasserburg et al., 2015).

Applying the internal $^{49}Ti/^{47}Ti$ normalization scheme used here for the leachates and CAIs to the presolar SiC grain data results in mean apparent Ti anomalies of $+704 \pm 47$ (2 s.e.) $\varepsilon^{46}Ti$, -396 ± 34 $\varepsilon^{48}Ti$, and $+503 \pm 84$ $\varepsilon^{50}Ti$ for mainstream SiC, and $+2071 \pm 1228$ $\varepsilon^{46}Ti$, -1674 ± 535 $\varepsilon^{48}Ti$, and -2688 ± 1123 $\varepsilon^{50}Ti$ for SiC X-grains (rare, most likely of supernova origin), respectively (Fig. 6). Mixing lines between terrestrial Ti and mainstream SiC have a negative slope in $\varepsilon^{48}Ti$ vs. $\varepsilon^{46}Ti$ and $\varepsilon^{48}Ti$ vs. $\varepsilon^{50}Ti$ space, and a positive slope for $\varepsilon^{50}Ti$ vs. $\varepsilon^{46}Ti$ (Fig. 6). In contrast to the SiC grains, hibonite-rich CAIs most commonly encountered in CM chondrites are thought to have mostly formed by condensation/evaporation processes in the nascent solar nebula. Hibonites exhibit more subdued anomalies in $\varepsilon^{46}Ti$ and $\varepsilon^{48}Ti$, but cover a range of ~3000 in $\varepsilon^{50}Ti$ (*e.g.*, Ireland, 1988; Kööp et al., 2016). Titanium anomalies in FUN CAIs are uncorrelated and restricted to a range of < 100 ε (Niederer et al., 1985; Kööp et al., 2018). "Normal" CAIs from CV, CO, CR, CK, and ordinary chondrites span a range of +2 to +15 $\varepsilon^{50}Ti$, with a prominent peak at about +9 $\varepsilon^{50}Ti$ (Leya et al., 2009; Trinquier et al., 2009; Davis et al., 2018; Ebert et al., 2018; Williams et al., 2016; Render et al., 2019). Furthermore, while significant scatter beyond analytical precision is seen in CAIs in $\varepsilon^{48}Ti$ vs. $\varepsilon^{46}Ti$, the anomalies in $\varepsilon^{46}Ti$ vs. $\varepsilon^{50}Ti$ in CAIs are well correlated ($R^2 = 0.74$) (Fig. 6).

The Ti isotope anomalies in the Murchison leachates are only marginally larger than the range covered by bulk bodies and CAIs. This indicates that in contrast to many other elements (see below) the leaching procedure applied here did not efficiently separate highly anomalous carriers relative to more normal Ti (Fig. 6). Nevertheless, the leachate data provide important information about the contributors to the intrinsic Ti isotopic heterogeneity of the Murchison

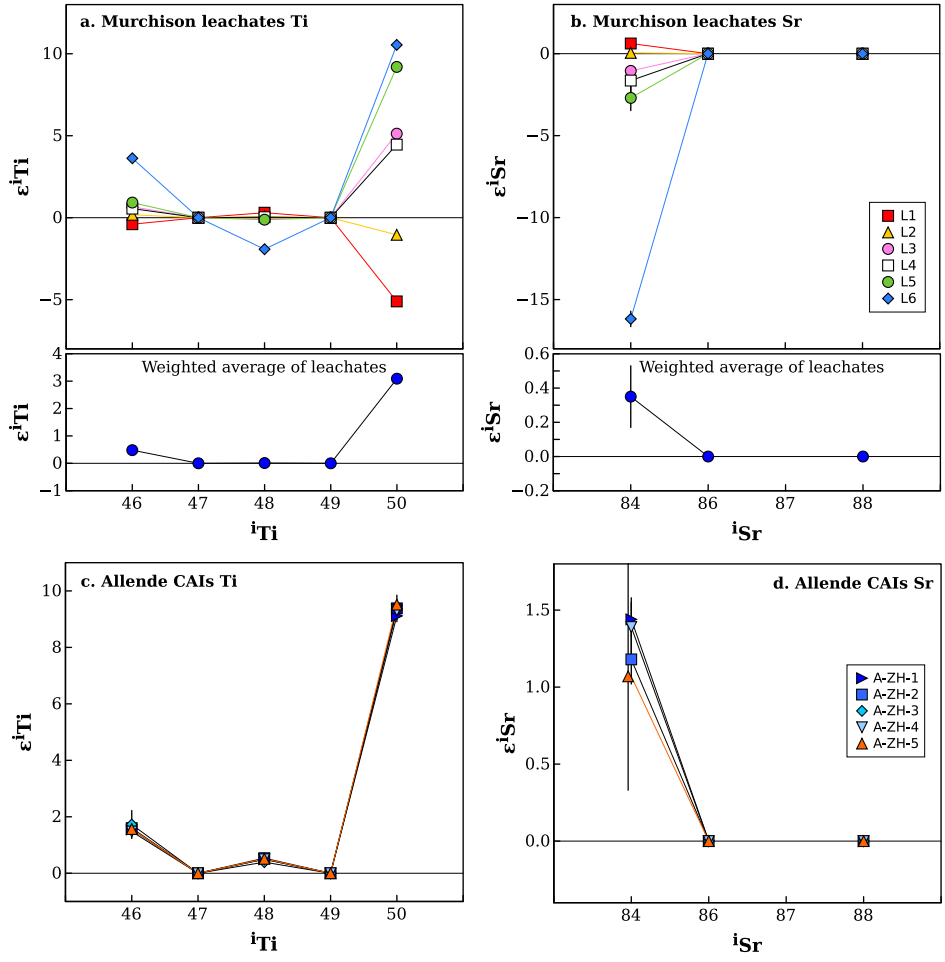

Fig. 4. Titanium and Sr isotopic anomaly data of Murchison leachates and Allende CAIs. (a,b) The leachate samples show variable nucleosynthetic Ti and Sr isotopic anomalies, the weighted average of which is consistent with bulk Murchison literature data. (c,d) Anomalies in the CAIs are homogeneous.

chondrite. In an ε^{46}Ti–ε^{48}Ti diagram, the leachate anomalies are negatively correlated, whereas in ε^{50}Ti vs. ε^{46}Ti space they are positively correlated; however, most of the leachates do not plot on the linear array defined by bulk planetary materials and CAIs. In ε^{i}Ti vs. ε^{j}Ti space, binary mixing follows a straight line, and so the Ti isotopic compositions of the different leachates reveals multiple contributors to the intrinsic Ti isotopic heterogeneity of the Murchison chondrite. The variations in ε^{46}Ti and ε^{48}Ti can be largely accounted for by progressive enrichment of mainstream SiC grains from L1 to L6 (Fig. 6a). In particular the Ti isotopic composition of the residue (L6) is clearly shifted towards mainstream SiC. This fraction is enriched in SiC grains, as these are chemically resistant to the acids used in leaching steps 1–5. All heavy elements with isotopes produced by the *p*-, *s*-, and *r*-processes (Mo, Ru, Ba, Sm) measured in L6 or equivalent, chemically resistant residues show *s*-process enrichments (Fig. 11d of Dauphas and Schauble, 2016), consistent with a large mainstream SiC contribution.

We note that CAIs with low ε^{46}Ti and ε^{50}Ti tend to have negative ε^{48}Ti anomalies, and thus some of the scatter in ε^{48}Ti in CAIs might be related to admixing of Ti from mainstream SiC (Fig. 6a, c). Accounting for potential mainstream SiC contribution in L6 leaves a large spread in ε^{50}Ti in the leachates, indicating that the main ε^{50}Ti variation is caused by one or multiple carriers with large ε^{50}Ti and subdued ε^{46}Ti and ε^{48}Ti variability. Hibonites are an obvious candidate with these features, but given their sub-solar Ca/Ti ratio, they cannot account for the 1:1 correlation between ε^{48}Ca and ε^{50}Ti observed for bulk meteorites. Presolar perovskite (Dauphas et al., 2014) or titanite ($CaTiSiO_5$) are potential alternative carriers.

In summary, and consistent with previous conclusions (Niederer et al., 1980; Trinquier et al., 2009; Steele and Boehnke, 2015; Davis et al., 2018), our leachate data reveal the contribution of at least three components with anomalous Ti isotopic compositions to the solar system's Ti isotopic inventory. The disparate leachate anomalies contrast with the linear correlation of bulk planetary bodies and

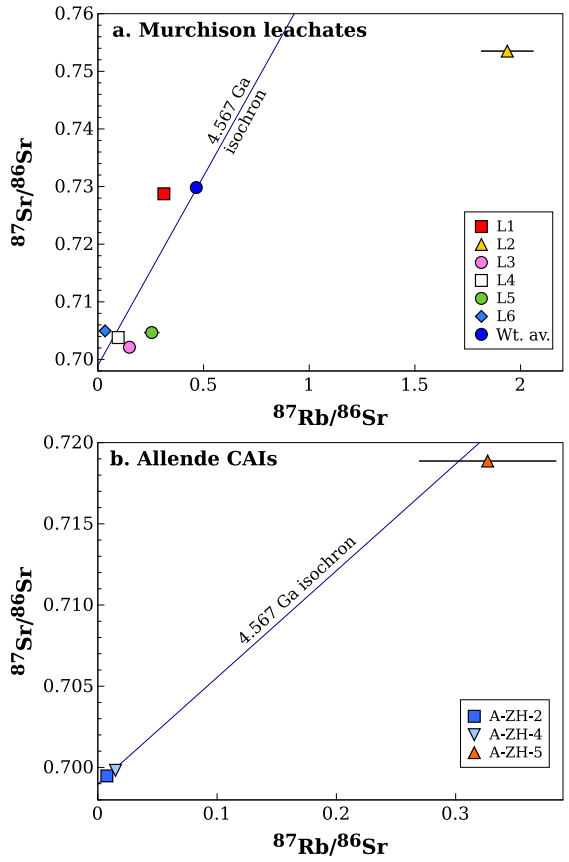

Fig. 5. ^{87}Rb-^{87}Sr isochron diagrams for Murchison leachates and Allende CAIs. (a) Individual leach steps show no isochronous relationship, while the weighted average of the leachates plots on a 4.567 Ga chondrite isochron. This indicates closed system evolution on the Murchison parent body, but incongruent dissolution of Rb and Sr during the leaching procedure. (b). Allende CAIs for which Rb/Sr and Sr isotopic composition data is available fall within uncertainty on a 4.567 Ga chondrite isochron.

CAIs in ε^{46}Ti – ε^{50}Ti space, indicating that the carriers responsible for the leachate anomalies most likely played only a minor, if any, role in the generation of the bulk meteorite and CAI anomalies. Since the Ti isotope anomalies in carbonaceous chondrites scale with the abundance of CAIs, the range of Ti anomalies in the CC reservoir is substantially reduced if CAIs are subtracted (Niemeyer, 1988; Leya et al., 2009; Trinquier et al., 2009; Burkhardt et al., 2016). For example, subtracting visible CAIs by mass-balance reduces the ε^{50}Ti anomaly of CV chondrites from ~+3.5 to ~+2.2 ε^{50}Ti (Burkhardt et al, 2016). This is similar to the anomaly of +1.85 ε^{50}Ti measured for CI chondrites, which contain no visible CAIs. The Ti isotopic variability among CC chondrites is, therefore, mainly controlled by the abundance of (still visible) CAIs in them. However, although the correction for the CAIs reduces the range of anomalies in the CC reservoir, a significant offset between the NC (ε^{50}Ti < 0) and CC (ε^{50}Ti > 1.85) reservoirs remains. Thus, this offset cannot be accounted for by the admixture of CAIs *sensu stricto*.

Chondrules from carbonaceous, ordinary, and enstatite chondrites (Gerber et al., 2017), together with chondrite matrix, bulk meteorites, and CAIs (Trinquier et al., 2009; Zhang et al., 2011) plot along a single ε^{46}Ti-ε^{50}Ti correlation line (Fig. 6b). Furthermore, chondrules from carbonaceous chondrites span a range between about −2 and +7 ε^{50}Ti, whereas EC and OC chondrules exhibit only limited scatter around their bulk meteorite Ti isotope compositions. The Ti isotope anomalies in the CC chondrules are correlated with their Ti concentration and size, while no such relation is observed in OC and EC chondrules. This was interpreted as evidence for the presence and heterogeneous distribution of CAI-like material among chondrule precursors in the formation region of carbonaceous chondrites (Gerber et al., 2017). These observations indicate that bulk carbonaceous chondrites do not only contain CAIs *sensu stricto*, but also reprocessed CAI-like material. Together, these two components exert a strong control on bulk planetary Ti isotope anomalies, and variable admixing of CAI-like refractory material to an average inner solar nebula component (as defined here by ECs and OCs) can account for a large part of the planetary-scale anomalies and the difference between non-carbonaceous (NC) and carbonaceous (CC) nebular reservoirs.

However, precisely quantifying the overall effect of CAI addition on Ti isotopic signatures in bulk carbonaceous chondrites is difficult, because the total amount of CAI-like material in individual chondrites is the sum of the visible CAIs plus the CAI-like material that was incorporated and reprocessed in chondrules and matrix. Moreover, the refractory dust involved may have had a chemical composition different from those measured in large CAIs. However, carbonaceous chondrites, including CI chondrites, are characterized by an excess of refractory lithophile elements relative to ECs and OCs (Grossman and Larimer, 1974; Wasson and Kallemeyn, 1988). Taking the Ti/Si ratio as a proxy for the excess refractory material in the CCs, we find that the ε^{50}Ti and Ti/Si of the bulk CCs are correlated, and plot on mixing lines between average ECs and OCs, and CAIs. The range of bulk scale Ti isotopic anomalies and Ti/Si ratios among carbonaceous chondrites can, therefore, entirely be accounted for by admixture of ~3–7% CAI-like material to an EC- or OC-like starting composition (Fig. 7a).

4.2. Strontium isotope anomalies in meteoritic materials

The four stable Sr isotopes have different contributions from the *p*-, *r*-, main *s*- and weak *s*-processes: ^{84}Sr is exclusively produced in the *p*-process; ^{86}Sr and ^{87}Sr are pure *s*-process nuclides (radiogenic ^{87}Rb with $t_{1/2}$ ~48 Gyr can be considered stable on the timescale of nucleosynthesis in stars during the lifetime of the Galaxy); and ^{88}Sr is produced by the *s*- and *r*-process (Arlandini et al., 1999). Most of the *s*-process Sr derives from AGB stars, but a fraction is also synthesized by the weak *s*-process in massive stars during the pre-supernovae stage (Woosley and Heger, 2007). The nature of the *r*-process in the Sr mass region is not well constrained, but when *r*-process is used in the following, it

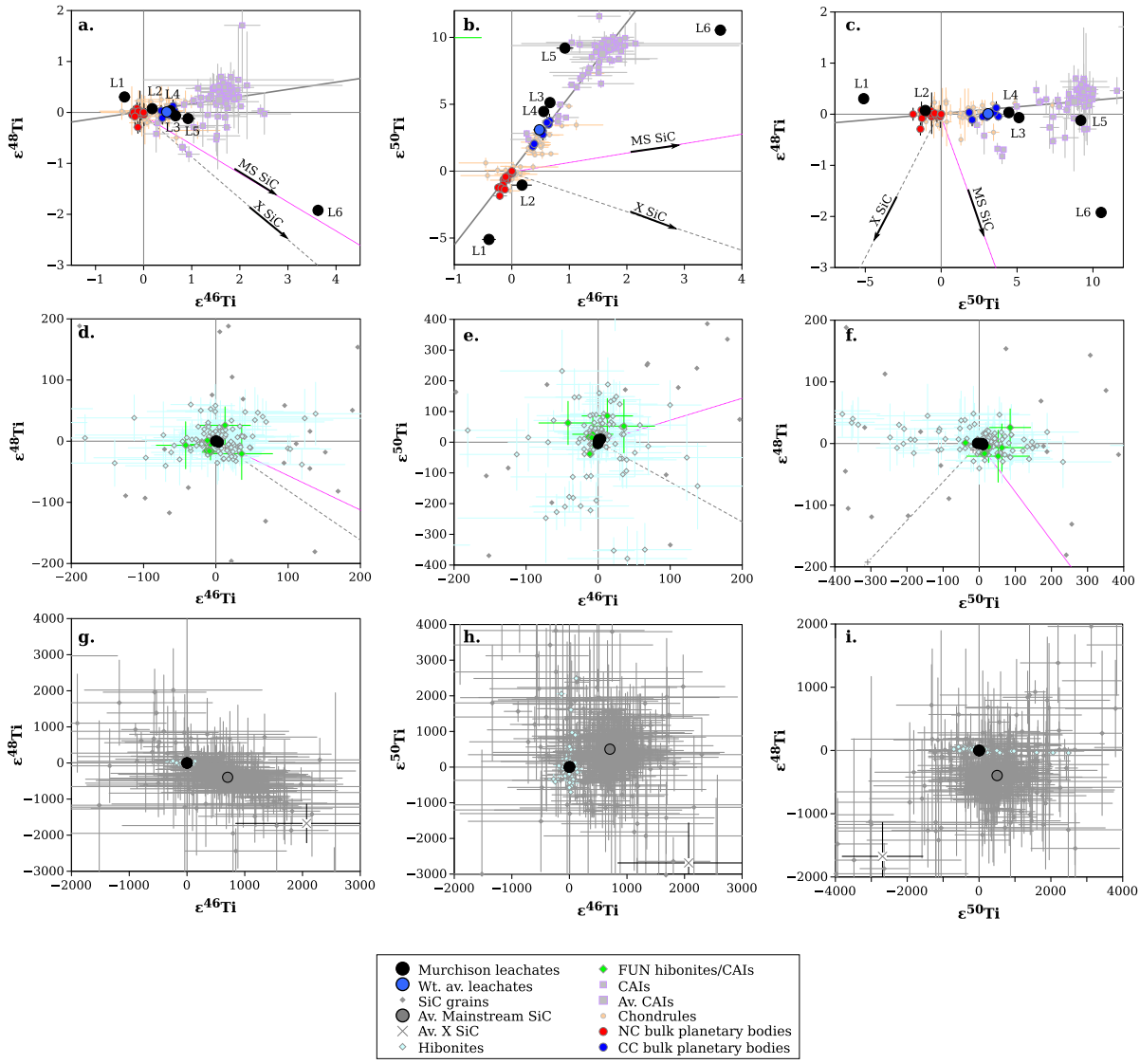

Fig. 6. Titanium isotope composition of Murchison leachates and various planetary materials in ε^{46}Ti, ε^{48}Ti, and ε^{50}Ti space. Anomalies vary by three orders of magnitude from presolar grains (panels g, h, i) via hibonites (panels d, e, f) to CAIs, individual chondrules, and bulk planetary bodies (panels a, b, c). For clarity, error bars of SiC grains were omitted in panels d, e, f.

refers to the *r*-residual after subtraction of the main *s*-process from the average solar system composition.

Strontium isotope data for SiC grains extracted from Murchison matrix reveal percent-level deficits in $^{84}Sr/^{86}Sr$, resulting from an enrichment in *s*-process ^{86}Sr relative to *p*-process ^{84}Sr in these presolar grains (Nicolussi et al., 1998; Podosek et al., 2004). The first evidence for mass-independent Sr isotope anomalies in material processed within the solar system was reported for FUN CAIs, which show deficits of ~–8 ε^{84}Sr and excesses of ~+32 ε^{84}Sr (Papanastassiou and Wasserburg, 1978) after normalization to a fixed $^{88}Sr/^{86}Sr$ ratio. "Normal" CAIs exhibit anomalies of about +1.3 in ε^{84}Sr (Moynier et al., 2012; Brennecka et al., 2013; Hans et al., 2013; Paton et al., 2013; Charlier et al., 2017; Myojo et al., 2018). Nucleosynthetic Sr isotope anomalies at the bulk meteorite scale seem to be restricted to CC bodies (Moynier et al., 2012; Hans et al., 2013; Paton et al., 2013; Yokoyama et al., 2015). At the current level of analytical precision, the Earth, Moon, Mars, eucrites, angrites, ECs, and OCs have indistinguishable relative abundances of non-radiogenic Sr isotopes, while carbonaceous chondrites exhibit slightly positive anomalies of up to +0.65 ε^{84}Sr (Fig. 7b). Note that for internally normalized Sr isotope data it is impossible to distinguish *p*-, *s*-, and *r*-process anomalies, because variations in ^{87}Sr are dominated by ^{87}Rb-decay, such that only three isotopes are left, two of which are used for internal normalization. Thus, the apparent variations in ε^{84}Sr seen in leachates, CAIs, and bulk bodies may be due to variations in either ^{84}Sr, ^{86}Sr, and ^{88}Sr, or a combination thereof. Double spike or sample-standard bracketing measurements are of little help because the isotopic anomalies in CAIs and

Table 4
Titanium and Sr isotope data of Allende CAIs.

CAI	Petrographic/chemical group	Rb [μg/g] ± 2σ	Sr [μg/g] ± 2σ	$^{87}Rb/^{86}Sr \pm 2\sigma$	$\varepsilon^{46}Ti^{a} \pm 2\sigma$	$\varepsilon^{48}Ti^{a} \pm 2\sigma$	$\varepsilon^{50}Ti^{a} \pm 2\sigma$	$\varepsilon^{84}Sr^{b} \pm 2\sigma$	$^{87}Sr/^{86}Sr \pm 2\sigma$
A-ZH-1	Coarse-grained Type B/group I				1.55 ± 0.11	0.49 ± 0.06	9.12 ± 0.13	1.44 ± 0.11	0.700674 ± 2E-06
A-ZH-2	Coarse-grained Type B/group I	*0.490*	*186.25*	*0.00760 ± 0.00005*	1.60 ± 0.07	0.53 ± 0.04	9.38 ± 0.11	*1.18 ± 0.2*	*0.699478 ± 3E-06*
A-ZH-3	Coarse-grained Type B/group I	1.95 ± 0.18	195 ± 29	0.0290 ± 0.0051	1.73 ± 0.50	0.39 ± 0.14	9.38 ± 0.47		
A-ZH-4	Coarse-grained Type B/group I	*0.70*	*137.10*	*0.01484 ± 9E-05*	1.48 ± 0.06	0.50 ± 0.05	9.31 ± 0.09	*1.39 ± 0.2*	*0.699821 ± 3E-06*
A-ZH-5	Fine-grained-Fluffy type A compound/group III	3.96 ± 0.36	35.0 ± 5.3	0.327 ± 0.057	1.57 ± 0.10	0.51 ± 0.04	9.51 ± 0.07	1.07 ± 0.74	0.718868 ± 6E-06

Values in italic are from Hans et al. (2013) and have been obtained after mild leaching of the CAIs in HCl to remove secondary Rb.

[a] $\varepsilon^{i}Ti = [(^{i}Ti/^{47}Ti)_{sample}/(^{i}Ti/^{47}Ti)_{OL\text{-}Ti} - 1] \times 10^{4}$ after mass-bias correction by internal normalization to $^{49}Ti/^{47}Ti = 0.749766$ using the exponential law. Uncertainties represent Student-t 95% confidence intervals $\sigma t_{0.95,n\text{-}1}/\sqrt{n}$.

[b] $\varepsilon^{i}Sr = [(^{i}Sr/^{86}Sr)_{sample}/(^{i}Sr/^{86}Sr)_{NBS\ 987} - 1] \times 10^{4}$ after mass-bias correction by internal normalization to $^{86}Sr/^{88}Sr = 0.1194$ using the exponential law. Uncertainties represent $2\sigma_{SE,mean}$.

bulk meteorites are small with regard to mass-dependent variations arising from evaporation/condensation processes or fluid alteration. Nevertheless, several lines of evidence suggest that the −16 $\varepsilon^{84}Sr$ anomaly of the insoluble residue (L6) reflects an excess in *s*-process isotopes. The insoluble residue of Murchison is enriched in presolar SiC produced in low mass AGB stars, and SiC grains reveal clear *s*-process signatures, including low $^{84}Sr/^{86}Sr$ ratios (Nicolussi et al., 1998; Podosek et al., 2004). Furthermore, isotopic analyses of residues remaining after dissolution of primitive chondrites reveal *s*-process enrichments for several elements, including Zr, Mo, Ba, W, and Os (Schönbächler et al., 2005; Qin et al., 2011; Burkhardt et al., 2012a; Burkhardt and Schönbächler, 2015; Elfers et al., 2018). Based on a comprehensive study of nucleosynthetic isotope anomalies in Murchison leachates, Qin et al. (2011) also concluded that the large $\varepsilon^{84}Sr$ deficits in the insoluble residue reflected an excess in *s*-process Sr. Likewise, leachate studies on the SiC-rich carbonaceous chondrites Ivuna (Paton et al., 2013), Murchison, and Tagish Lake (Yokoyama et al., 2015) obtained qualitatively similar results to those found here, while leachates of the slightly metamorphosed and SiC-poor Allende (Yokoyama et al., 2015) did not show significant $\varepsilon^{84}Sr$ variations.

Fig. 8 shows the $\varepsilon^{84}Sr$ values of the different leach steps in comparison to the $\varepsilon^{94}Mo$ values measured on the same aliquots. The $\varepsilon^{84}Sr$ and $\varepsilon^{94}Mo$ leachate anomalies are positively correlated, and roughly follow the expected covariation resulting from a variable distribution of *s*-process nuclides, calculated using the formalism of Dauphas et al. (2004) and the *s*-process abundances of Bisterzo et al. (2014) and Arlandini et al. (1999). Note, however, that the *s*-process yields in these publications are relevant only for the nucleosynthesis in AGB stars, but up to 20–40% of ^{87}Sr and ^{86}Sr is produced by the weak *s*-process (Woosley and Heger, 2007), while only 5% of ^{88}Sr was produced by this process (Travaglio et al., 2004). The acetic acid leachate (L1) plots significantly off the calculated $\varepsilon^{84}Sr$–$\varepsilon^{92}Mo$ *s*-process mixing line and has a much lower $\varepsilon^{84}Sr$ than expected for its $\varepsilon^{94}Mo$ (Fig. 8). This is likely the result of aqueous alteration on the parent body, whereby a large fraction of Sr from Murchison was mobilized and redistributed into carbonates (Riciputi et al., 1994) while the carrier(s) of Mo were less affected. In summary, the leachates provide evidence for intrinsic *s*-process Sr variability in Murchison, particularly in the later steps, whereas the early leach steps are dominated by Sr that has been homogenized by fluid mobilization on the parent body.

All CAIs investigated here are characterized by a positive $\varepsilon^{84}Sr$ anomaly, consistent with previously reported results for CAIs from CV3 (Moynier et al., 2012; Brennecka et al., 2013; Hans et al., 2013; Paton et al., 2013; Myojo et al., 2018) and CK3 (Shollenberger et al., 2018) chondrites. Thus, elevated $\varepsilon^{84}Sr$ seem to be a common feature of "normal" (*i.e.*, non-FUN) CAIs. As outlined above, positive $\varepsilon^{84}Sr$ may reflect either a *p*-excess, *r*-excess, or *s*-deficit (Papanastassiou and Wasserburg, 1978). Paton et al. (2013) interpreted the elevated $^{84}Sr/^{86}Sr$ of CAIs to be due to a deficit in *s*-process Sr, which these

Table 5
Concentration data used for producing Figs. 7, 9, 10.

	Reservoir	Si	Ca	Ti	Cr	Ni	Sr	Zr	Mo	Ru	Ba	Nd	Sm	Hf	W	Os
CI	CC	107,000	9220	458	2650	10,800	7.3	3.6	1.0	0.69	2.4	0.47	0.15	0.12	0.10	0.49
CM	CC	129,000	12,700	634	3050	12,000	10.1	8.0	1.3	0.88	3.3	0.63	0.20	0.19	0.14	0.64
CO	CC	159,000	15,800	780	3550	14,000	12.7	7.8	1.5	1.09	4.3	0.77	0.24	0.18	0.16	0.79
CV	CC	159,600	19,000	897	3600	13,400	16.0	8.3	1.5	1.13	4.9	0.97	0.31	0.19	0.19	0.83
OC mean	NC	175,000	13,000	620	3700	14,000	10.2	6.0	1.1	0.90	4.2	0.65	0.19	0.17	0.14	0.60
EC mean	NC	175,000	9200	510	3060	15,250	7.7	5.0	1.0	0.88	2.6	0.49	0.14	0.15	0.13	0.63
Av. CV3 CAIs	CAI	125,600	164,300	6042	200	900	100	40	3.5	5	30	14	4.54	1.2	1	9

Data sources are Wasson and Kallemeyn (1988), Stracke et al. (2012), Kleine et al. (2004), Burkhardt et al. (2008, 2011, 2016), Trinquier et al. (2009), Archer et al. (2014), and therein. Note that the elemental composition of different types of CAIs is variable (Stracke et al., 2012) and that the best estimates of the average CV3 CAI composition given here depend on the mix of inclusions.

authors inferred to reflect the formation of CAIs from essentially SiC-free material. In contrast, other studies argued that the positive ε^{84}Sr of CAIs is due to an excess in *r*-process Sr, since the same CAIs analyzed for Sr have been found to exhibit an *r*-process excess in the neighboring element Mo (Burkhardt et al., 2011; Brennecka et al., 2013). However, for Ru, which is the next neighboring element, the isotope anomalies in CAIs seem more consistent with *s*-process rather than *r*-process variations (Chen et al., 2010). CAI A-ZH-5 is particularly interesting in this respect, because although its ε^{84}Sr (and ε^{50}Ti) anomaly is within uncertainty identical to other "normal" CAIs, its Mo isotopic signature differs significantly (Burkhardt et al., 2011). In addition to an *r*-excess similar to that of other CAIs, A-ZH-5 exhibits a large *s*-process Mo deficit, which, when translated into a deficit in *s*-process Sr, would correspond to an ε^{84}Sr of ~+7.5, much higher than the observed value of ~+1.1 (Table 4). Thus, at least in terms of *s*-process variability, Mo and Sr isotope anomalies in CAIs can be decoupled. As such, the data for A-ZH-5 indicate that whereas the homogeneous enrichment in *r*-process material relative to the terrestrial composition is a common feature of the CAI-forming reservoir, the *s*-process variability in Mo is a secondary trait. These observations are fully consistent with inferences from Mo isotope anomalies at the bulk meteorite scale, which show that *s*-process Mo variability exists within the NC and CC reservoirs, whereas the offset between them is caused by an approximately homogeneous *r*-process excess in the CC over the NC reservoir (Budde et al., 2016; Kruijer et al., 2017; Poole et al., 2017; Worsham et al., 2017).

The ε^{84}Sr anomalies in CC bodies range from ~+0.4 in CI to ~+0.65 in CV chondrites, whereas terrestrial rocks, ECs, OCs, angrites, HEDs, as well as lunar and martian samples have indistinguishable non-radiogenic Sr isotopic compositions at the current level of analytical precision (Moynier et al., 2012; Hans et al., 2013; Paton et al., 2013; Yokoyama et al., 2015). As for Ti, the Sr isotopic composition of the carbonaceous chondrites and the offset between the NC and the CC reservoir is mainly controlled by CAIs (and reprocessed CAI-like matter). The range of bulk-scale Sr isotopic anomalies and Si/Sr ratios of CC bodies and their offset from the NC reservoir can be accounted for by admixture of ~4–10% of CAI-like materials to an EC- or OC-like starting composition (Fig. 7b).

4.3. Origin and relation of isotope anomalies in meteoritic components and bulk meteorites in multi-elemental parameter space

Due to continuous analytical progress it is now evident that chondrites display intrinsic nucleosynthetic isotopic variability in virtually every element investigated. The sequential digestion of carbonaceous chondrites revealed anomalies in Ca, Ti, Cr, Sr, Mo, Ru, Pd, Ba, Nd, Sm, Er, Yb, Hf, W, and Os isotopes, and only a handful of elements such as Cd, Sn, and Te evaded the clear detection of internal isotope anomalies thus far. For elements beyond the Fe-peak, the individual leachate data are all well explained by excesses and deficits in *s*-process isotopes (see Fig. 12 in

Table 6
Compilation of isotope anomalies in bulk planetary materials, average CV3 CAIs, and the weighted average of Murchison leachates.

	Reservoir	ε^{48}Ca	2σ	ε^{50}Ti	2σ	ε^{54}Cr	2σ	ε^{62}Ni	2σ	ε^{84}Sr	2σ	ε^{96}Zr	2σ	ε^{94}Mo	2σ	ε^{100}Ru	2σ	ε^{135}Ba	2σ	ε^{145}Nd	2σ	ε^{144}Sm	2σ	ε^{180}Hf	2σ	ε^{183}W	2σ	ε^{186}Os	2σ
Carbonaceous chond.																													
CI	CC	2.05	0.20	1.85	0.12	1.56	0.06	0.20	0.14	0.40	0.10	0.34	0.24	0.79	0.41	−0.24	0.13	0.27	0.14	−0.21	0.13	−1.02	0.46					0.13	0.17
CM	CC	3.14	0.14	3.01	0.10	1.02	0.08	0.10	0.03	0.40	0.09	0.76	0.37	4.03	1.43	−1.23	1.51	0.34	0.31	0.07	0.06	−0.65	0.66	−0.11	0.46	0.09	0.24	0.46	0.53
CO	CC	3.87	0.56	3.77	0.50	0.77	0.33	0.11	0.03	0.41	0.21	0.69	0.25	1.29	0.40	−0.92	1.22							0.01	0.40	0.02	0.15		
CV	CC	3.92	0.50	3.49	0.20	0.87	0.07	0.11	0.03	0.63	0.10	1.10	0.31	1.47	0.45	−1.17	0.22	0.26	0.41	0.03	0.05	−0.87	0.17	0.05	0.30	0.04	0.04	−0.24	0.14
CK	CC			3.63	0.40	0.48	0.30					0.45	0.25	1.55	0.36	−1.10	0.23							0.21	0.37	−0.07	0.17	−0.80	0.29
CR	CC	2.15	0.11	2.74	1.17	1.31	0.10	0.09	0.05			1.03	0.40	2.82	0.38	−0.76	0.45									0.38	0.19		
CH	CC					1.37	0.29							1.79	0.10	−0.91	0.13									0.12	0.17		
CB	CC			2.04	0.07	1.21	0.09	0.16	0.11			0.96	0.25	1.30	0.26	−1.04	0.13									0.10	0.15		
Ordinary chondrites																													
H	NC	−0.24	0.30	−0.64	0.17	−0.36	0.08	−0.06	0.03	−0.13	0.10	0.67	0.44	0.72	0.24	−0.27	0.04	0.08	0.13	0.05	0.03	0.06	0.06	0.11	0.40			0.18	0.12
L	NC	−0.32	0.03	−0.63	0.08	−0.40	0.10	−0.04	0.03	−0.11	0.21			0.66	0.39	−0.28	0.13	0.14	0.04	0.09	0.13	0.02	0.17	0.02	0.30				
LL	NC	−0.15	0.39	−0.67	0.08	−0.42	0.07	−0.07	0.03	−0.43	0.10	0.34	0.25	0.74	0.72	0.12	0.70	0.08	0.05	0.06	0.18	0.05	0.23	−0.1	0.27				
OC Mean	NC	−0.28	0.20	−0.65	0.07	−0.39	0.04	−0.06	0.02	−0.17	0.15	0.60	0.35	0.70	0.14	−0.24	0.06	0.10	0.05	0.06	0.03	0.05	0.05	0.07	0.20	0.09	0.17	0.18	0.12
Rumuruti chondrites																													
R	NC					0.16	0.50							0.42	0.10	−0.39	0.13							−0.35	0.50	−0.01	0.18		
Enstatite chondrites																													
EH	NC	−0.32	0.56	−0.14	0.07	0.04	0.08	0.03	0.03	−0.21	0.12	−0.02	0.30	0.59	0.36	−0.16	0.25	0.17	0.07	0.05	0.03	−0.02	0.13					−0.24	0.48
EL	NC	−0.38	0.26	−0.28	0.17	0.04	0.07	−0.03	0.07					0.36	0.09	−0.08	0.05			0.03	0.04	0.27	0.24					−0.38	0.41
EC Mean	NC	−0.37	0.46	−0.20	0.08	0.04	0.05	0.00	0.03	−0.21	0.12	−0.02	0.30	0.41	0.08	−0.08	0.03	0.17	0.07	0.04	0.02	0.00	0.08	−0.05	0.15			−0.31	0.44
Av. CV3 CAIs	CAI	3.80	1.33	8.77	0.53	7.00	1.00	1.00	0.30	1.26	0.11	1.61	0.31	1.23	0.19	−1.60	0.07	0.54	0.06	−0.23	0.03	−2.34	0.10	0.30	0.02	0.08	0.14	0.50	0.70
Wt. av. Murch. leach.	CC	3.25	0.23	3.10	0.17	1.63	0.10			0.35	0.18	1.03	0.68	3.37	0.30			0.61	0.29	0.05	0.06	−0.7	0.30	−0.57	0.22	0.12	0.42	1.65	1.44
Achondrites																													
Acapulcoites	NC			−1.30	0.05	−0.75	0.25							0.94	0.12											−0.06	0.17		
Lodranites	NC					−0.34	0.25							1.10	0.30											−0.09	0.13		
Brachinites	NC													1.12	0.15														
Winonaites	NC	−0.21	0.09											0.22	0.10														
NWA5363/5400	NC	−0.53	0.20	−1.01	0.10	−0.37	0.13	0.01	0.03					0.69	0.19	−0.34	0.13			0.11	0.06	0.27	0.43						
Angrites	NC	−1.06	0.33	−1.18	0.08	−0.43	0.15	0.01	0.05	0.00	0.10			0.75	0.11					−0.11	0.26					−0.06	0.09		
Aubrites	NC	−0.44	0.59	−0.06	0.11	−0.16	0.19	0.05	0.19					0.48	0.05														
HED	NC	−1.24	0.29	−1.23	0.05	−0.67	0.09	0.03	0.12	0.01	0.10	0.47	0.21					0.05	0.04	0.10	0.04					−0.03	0.13		
Ureilites	NC	−1.82	0.44	−1.85	0.26	−0.92	0.05	−0.04	0.10					0.89	0.09											0.00	0.04		
Mars' mantle	NC	−0.20	0.03	−0.43	0.06	−0.18	0.05	0.04	0.03	−0.25	0.15			0.37	0.10					−0.02	0.01					0.02	0.13		
Moon	NC	0.04	0.03	−0.03	0.04	0.15	0.10			−0.22	0.13															−0.01	0.15		
Earth mantle		0	0	0	0	0	0	0	0	−0.19	0.16	0.06	0.04	0	0	0	0	0	0	0	0	0	0	0	0	0	0	0	0
Mesosiderites	NC			−1.27	0.16	−0.69	0.11							1.04	0.08														
Pallasites																													
MG pal	NC			−1.37	0.08	−0.39	0.4							0.85	0.22	−0.45	0.29											~0	0.2
Eagle station Pal	CC					0.7	0.1							0.85	0.32													~0	0.2
Iron meteorites																													
IAB	NC													0.04	0.10	−0.06	0.07									−0.06	0.04	~0	0.2
IC	NC							−0.05	0.07					0.88	0.26	−0.38	0.13									−0.05	0.06		
IIAB	NC							−0.07	0.04					1.20	0.22	−0.46	0.05									−0.02	0.02	~0	0.2
IIC	CC							0.16	0.09					2.22	0.09	−1.04	0.05									0.28	0.07		
IID	CC							0.19	0.06					1.16	0.16	−1.04	0.13									0.11	0.07		
IIE	NC					−0.59	0.13							0.71	0.15														
IIF	CC							0.09	0.04					1.11	0.13	−0.99	0.13									0.09	0.02		
IIIAB	NC					−0.85	0.06	−0.11	0.07					1.07	0.24	−0.63	0.06									−0.03	0.02	~0	0.2
IIICD	NC													−0.06	0.32														
IIIE	NC							−0.07	0.06					1.01	0.14	−0.51	0.09									−0.05	0.04		
IIIF	CC							0.12	0.08					1.20	0.11	−0.99	0.13									0.08	0.07		
IVA	NC							−0.07	0.05					0.80	0.28	−0.29	0.09									−0.03	0.07	~0	0.2
IVB	CC							0.08	0.03					1.55	0.22	−0.90	0.05									0.13	0.02	~0	0.2

Classification of meteorites into NC and CC is based on isotopic dichotomy in Ti, Cr, and Mo isotopes (Trinquier et al., 2007; Leya et al., 2008; Warren, 2011; Budde et al., 2016). Uncertainties represent Student-t 95% confidence intervals $\sigma t_{0.95,n-1}/\sqrt{n}$. Note that for some elements (e.g., Ti; cf. Fig. 6) the isotopic composition measured for individual CAIs spans a significantly larger range than what is indicated by the 95%ci. This suggests admixing of NC material to CAIs at the level of individual inclusions, or spacial/temporal heterogeneities in the CAI forming reservoir. Data sources as in compilation by Burkhardt et al. (2017), with addition of Brennecka et al. (2013), Akram et al. (2013), Huang et al. (2012), Nanne et al. (2019), Schiller et al. (2018), Davis et al. (2018), Birck (2004), Kruijer et al. (2017), Worsham et al. (2017; 2019), Budde et al. (2018,2019), Walker (2012), Sprung et al. (2010), Yokoyama et al. (2007, 2010), and therein.

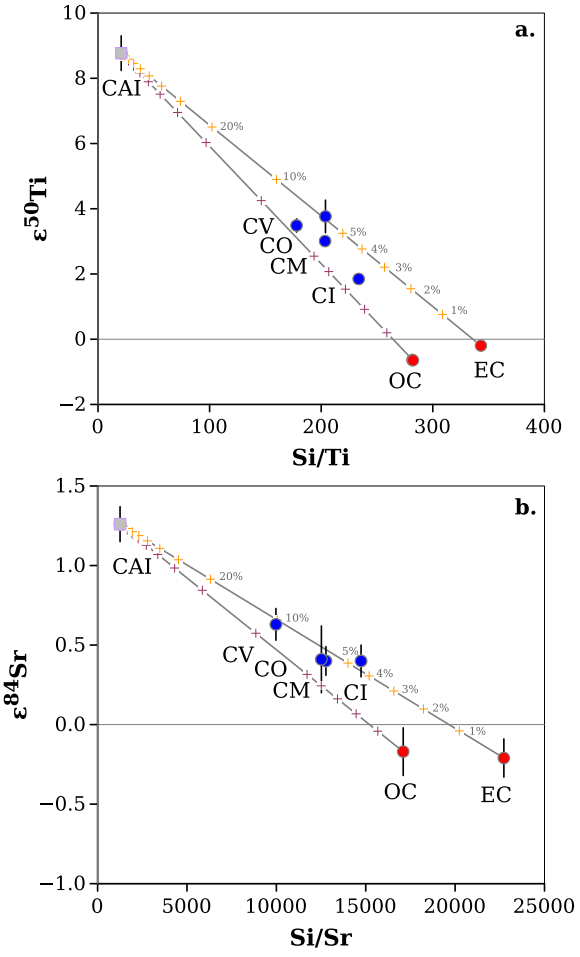

Fig. 7. Mixing diagrams of CAIs and average ordinary (OC) and enstatite chondrites (EC) for ε^{50}Ti vs. Si/Ti and ε^{84}Sr vs. Si/Sr. Carbonaceous chondrites (CC) fall along or between mixing trajectories. This indicates that the presence of several percent (by mass) of CAI-like refractory materials in CC bodies can satisfy both, the refractory element enrichment of CC relative to NC bodies, as well as the offset and variation in nucleosynthetic anomalies. Data used to construct diagrams are given in Tables 5 and 6.

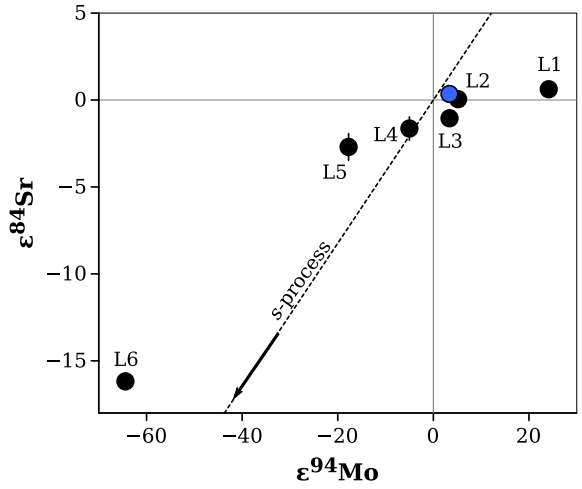

Fig. 8. ε^{84}Sr vs. ε^{94}Mo of leachates is positively correlated, and roughly follow the expected co-variation resulting from a variable distribution of *s*-process nuclides (dashed line, calculated using the formalism of Dauphas et al. (2004) and the *s*-process abundances of Bisterzo et al. (2014) and Arlandini et al. (1999). The acetic acid leachate (L1) plots significantly off the calculated ε^{84}Sr–ε^{92}Mo correlation line, indicating fluid-assisted Sr mobilization and redistribution on the parent body.

Dauphas and Schauble, 2016), highlighting that *s*-process carriers play an important role in explaining the intrinsic chondrite/nebular variability. When the data are shown in multi-elemental isotope space it becomes evident that different elements behave differently during circumstellar condensation of their presolar carriers, nebular and parent body processing, and leaching. This leads to variable element ratios in the carriers and the leachates and explains why the leachate anomalies are well correlated for some elements, but not for others (Burkhardt et al., 2012b). This can be seen in Fig. 9 in diagrams of ε^{50}Ti *vs.* ε^{48}Ca, ε^{54}Cr, ε^{84}Sr, ε^{96}Zr, ε^{94}Mo, ε^{100}Ru, ε^{135}Ba, ε^{145}Nd, ε^{144}Sm, ε^{180}Hf, ε^{183}W, and ε^{186}Os isotope anomalies in leachates and acid residues of the Murchison meteorite (equivalent diagrams with ε^{84}Sr and ε^{94}Mo on the abscissa are provided in supplementary Figs. S1 and S2). In these

Fig. 9. ε^{50}Ti vs. ε^{48}Ca, ε^{54}Cr, ε^{84}Sr, ε^{96}Zr, ε^{94}Mo, ε^{100}Ru, ε^{135}Ba, ε^{145}Nd, ε^{144}Sm, ε^{180}Hf, ε^{183}W, and ε^{186}Os isotope anomalies in leachates and acid residues of the Murchison meteorite along with bulk NC, CC and CAI data, mixing lines between OC (purple crosses), EC (orange crosses) and CAIs, and approximate trajectories of *s*-process mixing lines. The Ca, Ti, Cr, Sr, Mo, Ru, W, and Os Murchison leachate data were acquired from the same 6-step sequential digestion, Zr data are from a 5-step digestion (Schönbächler et al., 2005), and Ba, Nd, Sm, and Hf data are from a 4-step digestion (Qin et al., 2011). Titanium isotope anomalies of the leachates are well correlated with geochemically similar elements like Zr, Hf, Nd, as well as with Mo and W. The general trend is from a *s*-deficit in L1 to a *s*-excess in L6. Very poor, if any, correlation exists in the leachates for Ti and Ca, Cr, Ru, and Os although some of these elements like Ca and Ti show tight correlation at a bulk meteorite scale. The reason for the decoupling reflects that fact that these elements have different geochemical behaviors so that mixing between different mineral fractions tapped by the various leaching steps follow complex topologies in mixing spaces. The weighted average anomaly of the leachates is well within the range of bulk CC bodies for all elements analyzed. For no element pair the offset between NC and CC meteorites is clearly attributable to the correlations seen in the leachates, highlighting that the offset is decoupled from the dominant intrinsic anomalies as recorded in the leachates. For data sources see main text and Tables 5 and 6. Equivalent diagrams with ε^{84}Sr and ε^{94}Mo on the abscissa are provided in supplementary Figs. S1 and S2. (For interpretation of the references to colour in this figure legend, the reader is referred to the web version of this article.)

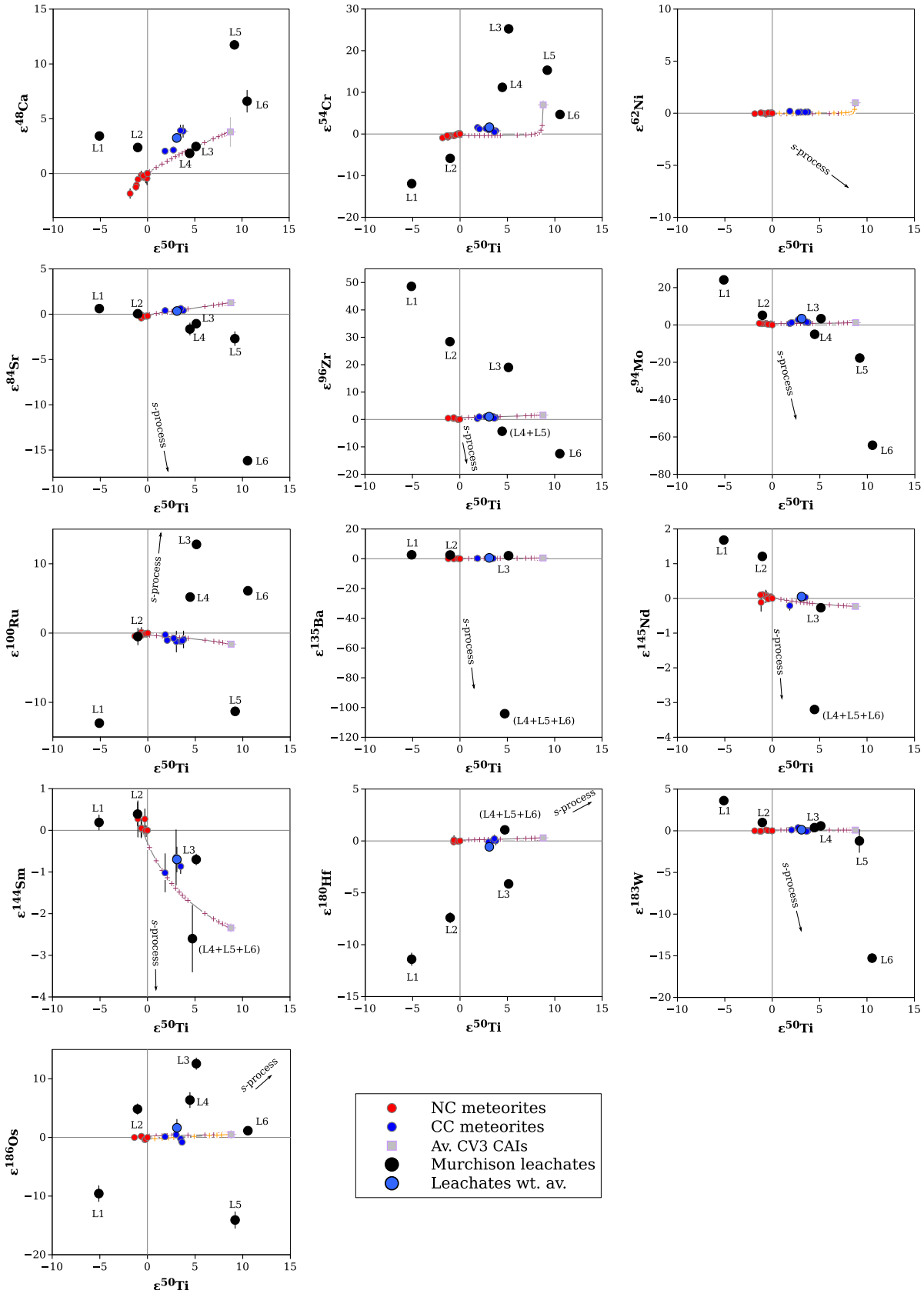
ε48Ca
ε50Ti
L1
L2
L3
L4
L5
L6
ε54Cr
ε62Ni
s-process
ε84Sr
ε96Zr
(L4+L5)
ε94Mo
ε100Ru
ε135Ba
(L4+L5+L6)
ε145Nd
ε144Sm
ε180Hf
ε183W
ε186Os
NC meteorites
CC meteorites
Av. CV3 CAIs
Murchison leachates
Leachates wt. av.

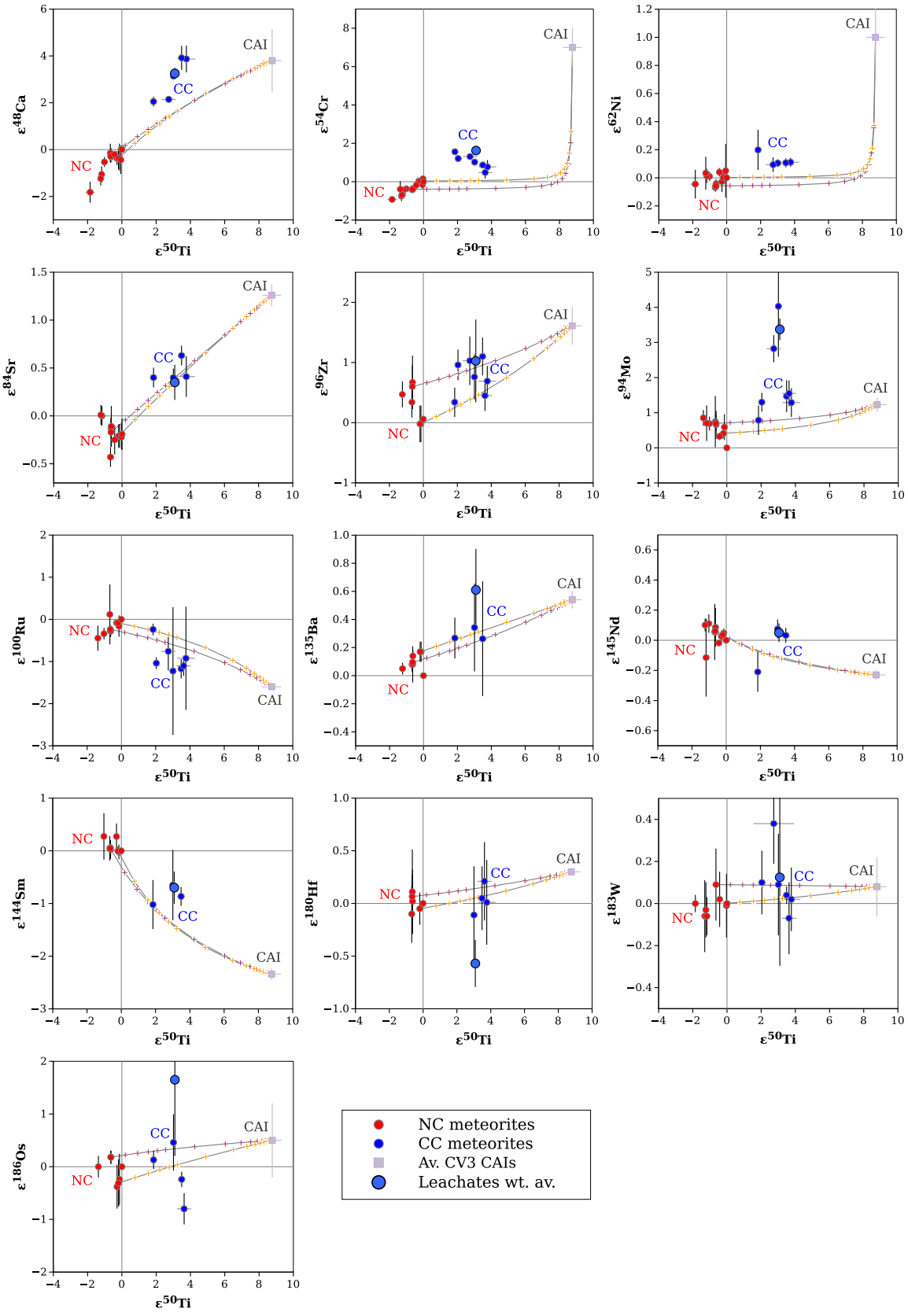
ε48Ca
ε50Ti
CAI
CC
NC
ε54Cr
ε62Ni
ε84Sr
ε96Zr
ε94Mo
ε100Ru
ε135Ba
ε145Nd
ε144Sm
ε180Hf
ε183W
ε186Os
NC meteorites
CC meteorites
Av. CV3 CAIs
Leachates wt. av.

diagrams, the shape of two-component mixing curves depends on the element concentration ratio in the mixing end-members. Only when the element ratio in both end-members is the same, the mixing curve is a straight line, in all other cases it is a hyperbola (Langmuir et al., 1978). Titanium isotope anomalies of the leachates are well correlated with isotope anomalies for geochemically similar elements like Zr, Hf, Nd, as well as with isotope anomalies for Mo and W. The general trend is from a *s*-deficit in L1 to an *s*-excess in the residue, suggesting common *s*-process carriers and limited fractionation of these elements during the leaching. Very poor, if any, correlation exists in the leachates for Ti and Ca, Cr, Ru, and Os although some of these elements, such as Ca and Ti, show tight correlations at the bulk meteorite scale (Dauphas et al., 2014; Schiller et al., 2015). The reason for the decoupling of leachate and bulk anomalies reflects the fact that these elements exhibit different geochemical and cosmochemical behavior, so that mixing between different mineral fractions tapped by the various leaching steps follow complex topologies in mixing space. Of note, the weighted average anomaly of the leachates is well within the range of bulk CC bodies for all elements analyzed. Furthermore, for no element pair can the offset between NC and CC meteorites be clearly attributed to the correlations seen in the leachates, further strengthening the observation that the NC-CC offset is decoupled from the dominant intrinsic anomalies as recorded in the leachates.

Instead, for many elements the CC meteorites are offset from the NC meteorites towards the composition of average CV3 CAIs. This can be seen in Fig. 10 (and supplementary Figs. S3 and S4), which is equivalent to Fig. 9 (and S1 and S2), but focused on the bulk and CAI anomalies. For the anomaly pairs ε^{50}Ti vs. ε^{84}Sr, ε^{96}Zr, ε^{135}Ba, and ε^{180}Hf the offset of NC and CC and the range within each reservoir is well-explained by admixing of CAIs to EC and OC compositions. For these elements the bulk anomalies are thus dominated by the presence of CAIs, and within group *s*-process variability is minor. For Mo, Ru, Nd significant nucleosynthetic *s*-process variability within the NC and/or the CC reservoirs exist (Dauphas et al., 2004; Carlson et al., 2007; Fischer-Gödde et al., 2015; Budde et al., 2016, 2019; Burkhardt et al., 2016), such that the location and range of the NC and CC meteorites in ε^{50}Ti vs. ε^{94}Mo, ε^{100}Ru, and ε^{145}Nd space is a function of both, *s*-process variability and variable addition of CAI-like material. This is consistent with what has been found based on Mo isotopes alone: the variability in NC and CC reservoirs is due to *s*-process heterogeneity, whereas the offset between the reservoirs is due to the homogeneous excess of *r*-process (*i.e.*, CAI-like) material in the CC reservoir (Budde et al., 2016; Poole et al., 2017; Kruijer et al., 2017; Worsham et al., 2017).

Importantly, the isotopic offset of CC bodies from the NC bodies towards average CV3 CAIs is not limited to refractory elements. For example, in ε^{50}Ti vs. ε^{54}Cr, and ε^{62}Ni space the CC bodies are offset from NC bodies towards the isotopic composition of CAIs for all three elements (Fig. 10). Since Cr and Ni are highly depleted in CAIs relative to bulk chondrites, the mixing hyperbolas of CAIs and EC and OC compositions have a strong curvature and do not encompass the CC bodies. CAIs *sensu stricto* are, therefore, not a viable component to explain the offset between NC and CC bodies for the main component elements Ni and Cr (Nanne et al., 2019). Nevertheless, the Ni and Cr isotopic compositions of the CC bodies are shifted toward the composition of CAIs. This suggests that CAIs are the refractory part of an isotopically distinct early nebular reservoir, and that the less refractory part of this reservoir with an approximately CAI-like isotopic signature also plays a role in setting planetary-scale isotope anomalies, including the offset between the NC and CC reservoirs. This is supported by the ε^{50}Ti vs. ε^{54}Cr correlation observed for NC bodies, which defines a straight line pointing toward the composition of CAIs, and could, as such, be explained by variable admixture of material characterized by a CAI-like isotopic composition, but with broadly solar chemical abundances.

In summary, for many elements the offset in nucleosynthetic anomalies between NC and CC bodies is largely decoupled from intrinsic *s*-process dominated variability, but is instead dominated by CAIs and isotopically CAI-like material. As can be seen in Fig. 10, the bulk meteorite anomalies within the NC and CC reservoirs can be along the same trajectory as the NC-CC offset, particular for elements that are strongly enriched in CAIs (*e.g.*, Ti, Sr), while for other elements (*e.g.*, Mo) the NC-CC offset and the within-reservoir variation follow different trends. Also, for some elements the main driver for within-reservoir variability is different for the NC and CC reservoirs, as is evident from disparate trajectories of NC and CC trends. Thus, planetary-scale nucleosynthetic isotope anomalies are the result of several, sometimes superimposed processes that acted on at least two initially isotopically distinct nebular reservoirs. In the following we discuss how these distinct nebular reservoirs might have formed, and propose a

Fig. 10. Like Fig. 9 but focused on the relation of anomalies in bulk NC and CC bodies, and CAIs. For the anomaly pairs ε^{50}Ti vs. ε^{84}Sr, ε^{96}Zr, ε^{135}Ba, and ε^{180}Hf the offset of NC and CC and the range within each reservoir is well-explained by admixing of CAIs to EC and OC compositions. For these elements the CAI anomalies are dominant and within group *s*-process variability is minor. For Mo, Ru, Nd significant nucleosynthetic *s*-process variability within the NC and/or the CC reservoirs have been demonstrated, such that the location and range of the NC and CC meteorites in ε^{50}Ti vs. ε^{94}Mo, ε^{100}Ru, and ε^{145}Nd space is a function of both, *s*-process variability and variable addition of CAI-like material. In ε^{50}Ti vs. ε^{54}Cr, and ε^{62}Ni space CC bodies are offset from NC bodies towards CAIs. However, since CAIs are depleted in Cr and Ni relative to bulk chondrites, mixing lines of CAIs and EC and OC compositions do not pass through the CC bodies. This suggests that CAIs are only the refractory part of an isotopically distinct nebular reservoir and less refractory material with ~CAI-like isotopic signature also plays a role in setting planetary scale anomalies. Equivalent diagrams with ε^{84}Sr and ε^{94}Mo on the abscissa are provided in supplementary Figs. S3 and S4. All panels and mixing lines can be reproduced with the data given in Tables 5 and 6.

potential scenario that can account for the elemental, isotopic, and structural diversity seen in planetary materials.

4.4. Origin of isotopically distinct nebular reservoirs: nebular processing or molecular cloud heterogeneity?

The main result of our analysis is that, although multiple processes contributed to the formation of planetary-scale isotopic heterogeneities, the difference between NC and CC bodies requires variable mixing between two isotopically distinct nebular reservoirs with approximately solar/-chondritic chemical compositions. One of these reservoirs is isotopically similar to CAIs (we call this hypothetical reservoir *IC* for Inclusion-like Chondritic component) and the other is more similar to the NC reservoir. As CAIs are the oldest dated objects that formed in the solar system, it is likely that this reservoir formed first, whereas the NC-like reservoir formed later. As to whether the isotopic difference between these two reservoirs reflects selective thermal processing of presolar carriers during infall or disk evolution, or is inherited from primordial variability in the solar system's parental molecular cloud is more difficult to assess. This is because we lack a complete inventory of the carriers of nucleosynthetic isotope anomalies that were initially present in the molecular cloud, making it difficult to even qualitatively assess how physico-chemical processing during infall or in the disk might have affected the isotopic composition of distinct disk reservoirs. Nevertheless, several observations suggest that the isotopic difference between the two early disk reservoirs is inherited from the solar system's parental molecular cloud, and does not result from thermal processing. First, the NC-CC offset is decoupled from the presolar carriers dominating the internal nucleosynthetic heterogeneity of meteorites, indicating that the NC-CC offset cannot easily be attributed to the heterogeneous distribution of presolar carriers that are still present in primitive meteorites. Second, the NC-CC offset is not limited to the signature of a single nucleosynthetic process, and so does not reflect processing of a specific presolar carrier. Instead, the CC reservoir is characterized by an enrichment in nuclides produced in neutron-rich stellar environments, which are hosted in distinct carriers. To account for this observation by thermal processing would therefore require preferential processing of a specific set of carriers, while other carriers (e.g., *s*-process carriers) would not have been affected. Thus, thermal processing could only account for the NC-CC offset under very specific assumptions. Third, thermal processing would have likely generated non-solar chemical compositions, but the generation of the NC-CC dichotomy requires mixing of two reservoirs with approximately solar concentration ratios. In our opinion, these observations are best explained if the NC-CC dichotomy is an inherited isotopic heterogeneity of the parental cloud that was preserved, in diluted form, during infall and subsequent mixing and processing within the disk.

The Sun most likely formed in a stellar cluster (Adams, 2010; Levison et al., 2010), and the presence and abundance of short-lived nuclides (in particular ^{26}Al) in early solar system materials requires the addition of freshly synthesized supernova or Wolf-Rayet star-material shortly before or during the collapse of the molecular cloud core (e.g., Gaidos et al., 2009; Dwarkadas et al., 2017). Given these constraints it is conceivable that in this dynamic environment the isotopic composition of the collapsing cloud material varied at the scale of the cloud core, and dynamical simulations, albeit of coarse resolution, suggest that initial cloud heterogeneities can survive in the forming disk (Visser et al., 2009). The lack of ^{26}Al in hibonite grains with large Ti and Ca isotope anomalies has been related to such cloud heterogeneities (Kööp et al., 2016). Thus, although it cannot be excluded that processing during infall or disk evolution contributed to the observed isotopic heterogeneities, our preferred interpretation for the origin of the two isotopically distinct nebular reservoirs and, hence, the NC-CC isotopic offset, is a change in the isotopic composition of the infalling cloud material.

4.5. Qualitative model for isotopic and elemental heterogeneities in the early solar system

Taking recent infall and disk evolution models (Yang and Ciesla, 2012; Pignatale et al., 2018), the proposed formation location of CAIs near the young Sun, and the early formation of CAIs as a guide, we infer that the molecular cloud parcel with the CAI-like isotopic composition represents early infalling material, whereas the molecular cloud parcel with an NC-like isotopic composition represents later infalling material. The change in infall and associated disk evolution is qualitatively sketched in Fig. 11 (a similar model was proposed in Nanne et al., 2019). Because early infall is limited to regions close to the star, and the forming disk is rapidly expanding through viscous spreading, variably processed cloud materials with CAI-like isotope composition (including CAIs *sensu strictu*, as well as less refractory dust) will be transported outwards, or condensed during the outward transport of hot nebular gas (Fig. 11a). This process can account for the overabundance of refractory phases in outer solar system materials (Yang and Ciesla, 2012). During further infall the centrifugal radius of infalling material is expanding, and the primary signature of the early infall will be diluted (Fig. 11b). The dilution is highest in the inner part of the disk, because throughout accretion the mass fraction of infalling material is always highest close to the star. Thus, the isotopic signature of the later infalling NC material will dominate the inner part of the disk. By contrast, the outer disk retains a higher fraction of matter from the earliest disk (*i.e.*, with a CAI-like isotopic composition), and, because of the outward expansion of the centrifugal radius also receives a higher fraction of unprocessed primitive cloud material. Subsequent transport, mixing, and processing of material in the disk reduced the initial isotopic difference between the two early disk reservoirs to the observed NC-CC offset, and led to the generation of secondary features like the *s*-process variability in the NC and CC reservoirs. A strength of this model is that it naturally explains many of the observables in the meteorite record: the excess of refractory elements and the higher amount of unprocessed material in the CC reservoir; the higher relative abundance of SiC

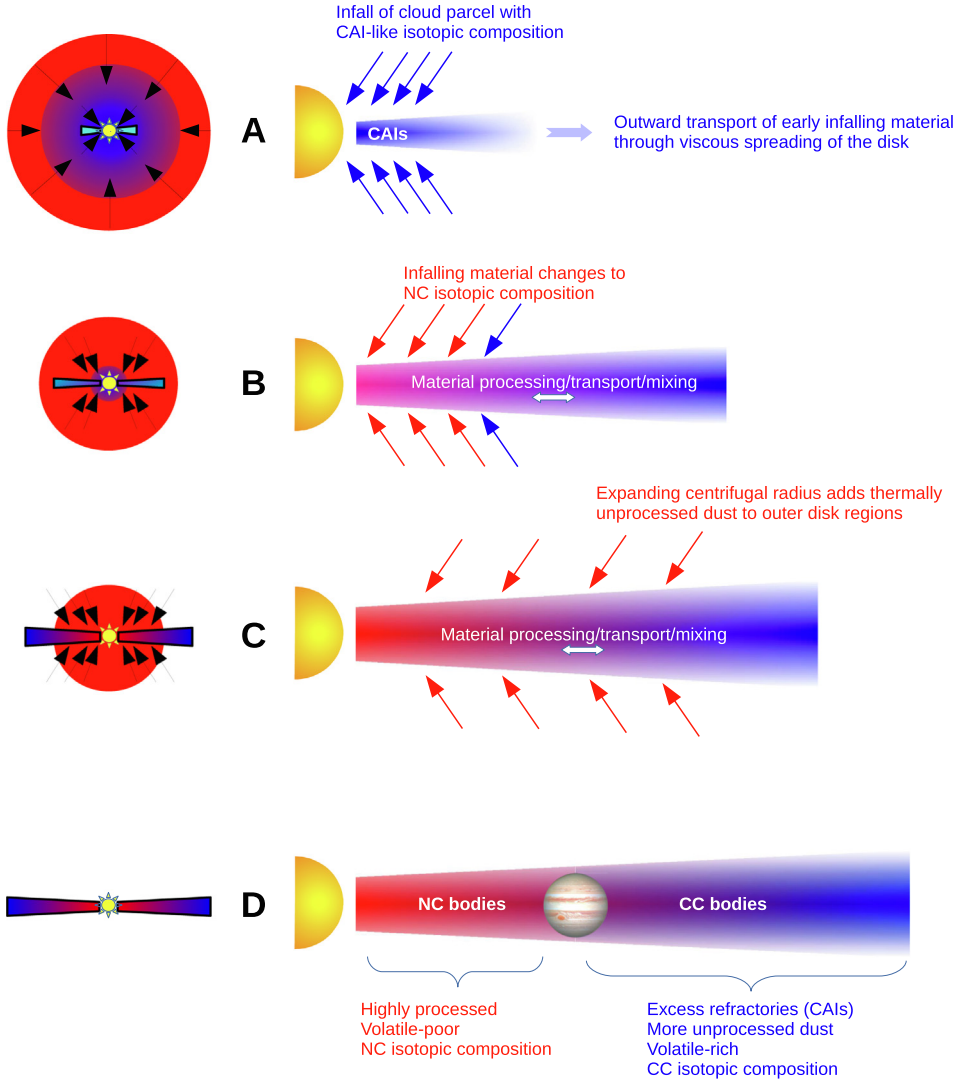

Fig. 11. A qualitative model of the early Solar System that accounts for key observables in the meteoritic record. The general set-up is adopted from Yang and Ciesla (2012) and Pignatale et al. (2018), but now the collapsing cloud core contains isotopically slightly distinct parcels, one with a CAI-like isotopic composition and one with a NC-like isotopic composition. (A) The initial stages of collapse are dominated by the isotopically CAI-like cloud parcel and the centrifugal radius of the infall is limited to regions close to the forming star *i.e.*, most of the material is processed at high temperatures. Through viscous spreading of the forming disk, this early infalling material is rapidly transported outwards. This process has been suggested to explain the overabundance of refractory phases in outer Solar System materials (Yang and Ciesla, 2012). (B) The centrifugal radius of infalling material is expanding with time, and the primary signature of the early infall will be diluted by the addition of NC cloud material, particularly in the inner disk regions. (C) Although material processing and transport in the disk will further dilute and mix the initial isotopic signatures, the outer disk retains a higher fraction of matter from the isotopically CAI-like reservoir, and also receives a higher fraction of unprocessed primitive cloud material. (D) At the end of infall the inner part of the disk contains high amounts of highly processed, volatile-poor material with an NC signature, while the outer disk has an excess in refractories from the early infall, a higher portion of unprocessed primitive dust, higher volatile contents, and an isotopic composition between NC and CAIs. This early set dichotomy was retained throughout accretion, possibly assisted by the early formation of Jupiter (Kruijer et al., 2017).

X grains to mainstream SiC grains in CC relative to NC chondrites (Lin et al., 2002); the presence of isotopically NC-like material with CAI-like condensation features in NC chondrites (Ebert et al., 2018); and the distinct isotopic compositions of the NC and CC reservoirs.

In our model, the isotopic composition of CAIs (which puzzled cosmochemists for decades because it cannot be related to a specific nucleosynthetic process for all elements) simply reflects the average composition of the early infalling molecular cloud material. In this framework, the similar O isotopic composition of the Sun and CAIs (McKeegan et al., 2011) are easily understood, because both formed predominately from the early infalling material. Obviously, while our two-component mixing scenario can explain many features of the elemental and isotopic meteorite record, it is only a simplified model of the processes that acted at the beginning of the solar system. Most likely the average CAI-like isotopic composition itself is a mixture

of molecular cloud parcels, and even earlier infalling material may have had a different composition (*e.g.*, ^{26}Al-free hibonites and FUN CAIs likely represent this even earlier-infalling material). However, the importance of these materials for understanding the isotopic variations among bulk meteorites is marginal. Therefore, based on our inferences the following testable prediction can be made: *for elements that do not show large systematic isotope anomalies in normal CAIs there will be no systematic offset between NC and CC meteorites*.

5. CONCLUSIONS

By systematically investigating the isotopic record of planetary materials in multi-element space, we evaluate the main controlling factors for the formation of planetary-scale nucleosynthetic isotope anomalies, and how these anomalies may relate to an isotopic heterogeneity of the solar system's parental molecular cloud. We find that the intrinsic (i.e., within-meteorite heterogeneity) isotope anomalies as sampled by acid leachates of primitive chondrites played only a minor, if any, role in the generation of Ti isotope anomalies in bulk meteorites and CAIs. We show instead that the Ti and Sr elemental and isotopic compositions of carbonaceous chondrites, and the isotopic offset between the NC and CC reservoir for these two elements, is mainly controlled by CAIs and reprocessed CAI-like material.

By expanding our analysis to other elements, we find that although the nucleosynthetic heterogeneity within the NC and CC reservoirs may have had variable origins (including nebular processing of *s*-process material), the systematic isotopic offset of the CC reservoir from the NC reservoir towards the composition of CAIs is a global feature and is not limited to refractory elements. This implies that the CC reservoir formed by mixing of two disk reservoirs having chondritic/solar chemical, but distinct isotopic compositions. In our preferred model, the isotopic difference between these two early disk reservoirs is a primordial feature that has been inherited from the solar system's parental molecular cloud during infall, whereby the early-infalling material was characterized by an approximately CAI-like isotopic composition (labeled IC for Inclusion-like Chondritic component), whereas later-infalling material had an NC-like isotopic composition. Subsequent mixing and processing within the disk resulted in additional isotopic variations within both reservoirs, and reduced the initial isotopic difference between them to the observed NC-CC isotopic offset. Planetary-scale nucleosynthetic isotope anomalies are, therefore, related to both, changes in the isotopic composition of the infalling material—ultimately leading to the isotopic offset between the NC and CC reservoirs—*and* differential processing and transport in the evolving circum-solar disk, resulting in isotopic variations within both reservoirs.

ACKNOWLEDGMENTS

We are grateful to the Field Museum for providing the Murchison sample, and thank A. Meibom, H. Palme, and an anonymous reviewer for editorial handling and constructive comments. Also, we thank L. Kööp for sharing hibonite data. This study was supported by SNSF grant (PBE2PZ-145946) to CB, SNSF grant (200021-113625) to BB, NASA grants 359NNX17AE86G (LARS), NNX17AE87G (Emerging Worlds), and 80NSSC17K0744 360 (Habitable Worlds) to ND, and by the European Research Council Consolidator Grant 'ISOCORE' to T. K. (contract no. 616564).

AUTHOR CONTRIBUTIONS

Element concentration and Ti isotope data were obtained by CB, Sr isotope data by UH under BB supervision. ND prepared the Murchison leachates, and encouraged CB to make use of the acquired data. CB interpreted the data, compiled literature data, performed calculations, and wrote the manuscript. The conceptual disk evolution model developed during discussions between TK and CB. All authors commented on the manuscript.

APPENDIX A. SUPPLEMENTARY MATERIAL

Supplementary data to this article can be found online at https://doi.org/10.1016/j.gca.2019.07.003.

REFERENCES

Adams F. C. (2010) The birth environment of the solar system. *Ann. Rev. Astron. Astrophys.* **48**, 47–85.

Akram W., Schönbächler M., Bisterzo S. and Gallino R. (2015) Zirconium isotope evidence for the heterogeneous distribution of s–process materials in the solar system. *Geochim. Cosmochim. Acta* **165**, 484–500.

Akram W., Schönbächler M., Sprung P. and Vogel N. (2013) Zirconium-Hafnium isotope evidence from meteorites for the decoupled synthesis of light and heavy neutron-rich nuclei. *Astrophys. J.* **777**, 169.

Alexander C. M. O. and Nittler L. R. (1999) The galactic evolution of Si, Ti, and O Isotopic ratios. *Astrophys. J.* **519**, 222–235.

Archer G. J., Ash R. D., Bullock E. S. and Walker R. J. (2014) Highly siderophile elements and ^{187}Re-^{187}Os isotopic systematics of the Allende meteorite: Evidence for primary nebular processes and late-stage alteration. *Geochim. Cosmochim. Acta* **131**, 402–414.

Arlandini C., Käppeler F. and Wisshak K. (1999) Neutron capture in low-mass asymptotic giant branch stars: cross sections and abundance signatures. *Astrophys. J* **525**, 886–900.

Birck J. L. (2004) An overview of isotopic anomalies in extraterrestrial materials and their nucleosynthetic heritage. *Rev. Mineral. Geochem.* **55**, 25–64.

Bisterzo S., Travaglio C., Gallino R., Wiescher M. and Käppeler F. (2014) Galactic chemical evolution and solar s-process abundances: Dependence on the ^{13}C-pocket structure. *Astrophys. J* **787**, 10.

Bizzarro M., Ulfbeck D., Trinquier A., Thrane K., Connelly J. N. and Meyer B. S. (2007) Evidence for a late supernova injection of Fe-60 into the protoplanetary disk. *Science* **316**, 1178–1181.

Boyet M., Bouvier A., Frossard P., Hammouda T., Garçon M. and Gannoun A. (2018) Enstatite chondrites EL3 as building blocks for the Earth: The debate over the ^{146}Sm–^{142}Nd systematics. *Earth Planet. Sci. Lett.* **488**, 68–78.

Boynton W. V. (1975) Fractionation in the solar nebula: condensation of yttrium and the rare earth elements. *Geochim. Cosmochim. Acta* **39**, 569–584.

Brennecka G. A., Borg L. E. and Wadhwa M. (2013) Evidence for supernova injection into the solar nebula and the decoupling of r-process nucleosynthesis. *Proc. Natl. Acad. Sci.* **110**, 17241–17246.

Budde G., Burkhardt C., Brennecka G. A., Fischer-Gödde M., Kruijer T. S. and Kleine T. (2016) Molybdenum isotopic evidence for the origin of chondrules and a distinct genetic heritage of carbonaceous and non-carbonaceous meteorites. *Earth Planet. Sci. Lett.* **454**, 293–303.

Budde G., Burkhardt C. and Kleine T. (2019) Molybdenum isotopic evidence for the late accretion of outer Solar System material to Earth. *Nat. Astron*. https://doi.org/10.1038/s41550-019-0779-y.

Budde G., Kruijer T. S. and Kleine T. (2018) Hf-W chronology of CR chondrites: Implications for the timescales of chondrule formation and the distribution of ^{26}Al in the solar nebula. *Geochim. Cosmochim. Acta* **222**, 284–304.

Burkhardt C., Borg L. E., Brennecka G. A., Shollenberger Q. R., Dauphas N. and Kleine T. (2016) A nucleosynthetic origin for the Earth's anomalous ^{142}Nd composition. *Nature* **537**, 394–398.

Burkhardt C., Dauphas N., Tang H., Fischer-Gödde M., Qin L., Chen J. H., Rout S. S., Pack A., Heck P. R. and Papanastassiou D. A. (2017) In search of the Earth-forming reservoir: Mineralogical, chemical, and isotopic characterizations of the ungrouped achondrite NWA 5363/NWA 5400 and selected chondrites. *Meteorit. Planet. Sci.* **52**, 807–826.

Burkhardt C., Kleine T., Dauphas N. and Wieler R. (2012a) Nucleosynthetic tungsten isotope anomalies in acid leachates of the Murchison chondrite: implications for Hf-W chronometry. *Astrophys. J. Lett.* **753**, L6.

Burkhardt C., Kleine T., Dauphas N. and Wieler R. (2012b) Origin of isotopic heterogeneity in the solar nebula by thermal processing and mixing of nebular dust. *Earth Planet. Sci. Lett.* **357–358**, 298–307.

Burkhardt C., Kleine T., Oberli F., Pack A., Bourdon B. and Wieler R. (2011) Molybdenum isotope anomalies in meteorites: Constraints on solar nebula evolution and origin of the Earth. *Earth Planet. Sci. Lett.* **312**, 390–400.

Burkhardt C., Kleine T., Palme H., Bourdon B., Zipfel J., Friedrich J. and Ebel D. (2008) Hf-W mineral isochron for Ca, Al-rich inclusions: Age of the solar system and the timing of core formation in planetesimals. *Geochim. Cosmochim. Acta* **72**, 6177–6197.

Burkhardt C. and Schönbächler M. (2015) Intrinsic W nucleosynthetic isotope variations in carbonaceous chondrites: Implications for W nucleosynthesis and nebular vs. parent body processing of presolar materials. *Geochim. Cosmochim. Acta* **165**, 361–375.

Carlson R. W., Boyet M. and Horan M. F. (2007) Chondrite barium, neodymium, and samarium isotopic heterogeneity and early earth differentation. *Science* **316**, 1175–1178.

Charlier B. L. A., Tissot F. L. H. and Dauphas N. (2017) Strontium stable isotope composition of allende fine-grained inclusions. In *Lunar and Planetary Science Conference*, vol. 48, p. 2352. Lunar and Planetary Science Conference.

Chen J. H., Papanastassiou D. A. and Dauphas N. (2011) Anomalous Ca Isotopic Compositions in Leachates of Murchison. In *Lunar and Planetary Science Conference*, vol. 42, p. 2440. Lunar and Planetary Science Conference.

Chen J. H., Papanastassiou D. A. and Wasserburg G. J. (2010) Ruthenium endemic isotope effects in chondrites and differentiated meteorites. *Geochim. Cosmochim. Acta* **74**, 3851–3862.

Clayton D. D. (1982) Cosmic chemical memory - a new astronomy. *Quat. J. Roy. Astron. Soc.* **23**, 174.

Clayton R. N., Onuma N. and Mayeda T. K. (1976) A classification of meteorites based on oxygen isotopes. *Earth Planet. Sci. Lett.* **30**, 10–18.

Dauphas N. (2005) The U/Th production ratio and the age of the Milky Way from meteorites and Galactic halo stars. *Nature* **435**, 1203–1205.

Dauphas N. (2017) The isotopic nature of the Earth's accreting material through time. *Nature* **541**, 521–524.

Dauphas N., Chen J. H., Zhang J., Papanastassiou D. A., Davis A. M. and Travaglio C. (2014) Calcium-48 isotopic anomalies in bulk chondrites and achondrites: Evidence for a uniform isotopic reservoir in the inner protoplanetary disk. *Earth Planet. Sci. Lett.* **407**, 96–108.

Dauphas N., Davis A. M., Marty B. and Reisberg L. (2004) The cosmic molybdenum-ruthenium isotope correlation. *Earth Planet. Sci. Lett.* **226**, 465–475.

Dauphas N., Marty B. and Reisberg L. (2002) Molybdenum evidence for inherited planetary scale isotope heterogeneity of the protosolar nebula. *Astrophys. J.* **565**, 640–644.

Dauphas N., Remusat L., Chen J. H., Roskosz M., Papanastassiou D. A., Stodolna J., Guan Y., Ma C. and Eiler J. M. (2010) Neutron-rich chromium isotope anomalies in supernova nanoparticles. *Astrophys. J.* **720**, 1577–1591.

Dauphas N. and Schauble E. A. (2016) Mass fractionation laws, mass-independent effects, and isotopic anomalies. *Annu. Rev. Earth Planet. Sci.* **44**, 709–783.

Davis A. M. and Grossman L. (1979) Condensation and fractionation of rare earths in the solar nebula. *Geochim. Cosmochim. Acta* **43**, 1611–1632.

Davis A. M., Zhang J., Greber N. D., Hu J., Tissot F. L. and Dauphas N. (2018) Titanium isotopes and rare earth patterns in CAIs: Evidence for thermal processing and gas-dust decoupling in the protoplanetary disk. *Geochim. Cosmochim. Acta* **221**, 275–295.

Dwarkadas V. V., Dauphas N., Meyer B., Boyajian P. and Bojazi M. (2017) Triggered star formation inside the shell of a Wolftextendash Rayet bubble as the origin of the solar system. *Astrophys J* **851**, 147.

Ebert S., Render J., Brennecka G. A., Burkhardt C., Bischoff A., Gerber S. and Kleine T. (2018) Ti isotopic evidence for a non-CAI refractory component in the inner solar system. *Earth Planet. Sci. Lett.* **498**, 257–265.

Elfers B.-M., Sprung P., Pfeifer M., Wombacher F., Peters S. T. M. and Münker C. (2018) Variable distribution of s-process Hf and W isotope carriers in chondritic meteorites - Evidence from ^{174}Hf and ^{180}W. *Geochim. Cosmochim. Acta* **239**, 346–362.

Fegley B. and Palme H. (1985) Evidence for oxidizing conditions in the solar nebula from Mo and W depletions in refractory inclusions in carbonaceous chondrites. *Earth Planet. Sci. Lett.* **72**, 311–326.

Fischer-Gödde M., Burkhardt C., Kruijer T. S. and Kleine T. (2015) Ru isotope heterogeneity in the solar protoplanetary disk. *Geochim. Cosmochim. Acta* **168**, 151–171.

Fischer-Gödde M., Kleine T., Burkhardt C. and Dauphas N. (2014) Origin of nucleosynthetic isotope anomalies in bulk meteorites: evidence from coupled Ru and Mo isotopes in acid leachates of chondrites. In *Lunar and Planetary Science Conference*, vol. 45, p. 2409. Lunar and Planetary Science Conference.

Gaidos E., Krot A. N., Williams J. P. and Raymond S. (2009) ^{26}Al and the formation of the solar system from a molecular cloud contaminated by Wolf-Rayet winds. *Astrophys. J* **698**, 1854.

Gerber S., Burkhardt C., Budde G., Metzler K. and Kleine T. (2017) Mixing and transport of dust in the early solar nebula as

inferred from titanium isotope variations among chondrules. *Astrophys. J. Lett.* **841**, L17.
Grossman L. and Larimer J. W. (1974) Early chemical history of the solar system. *Rev. Geophys.* **12**, 71–101.
Gyngard F., Amari S., Zinner E. and Marhas K. K. (2018) Correlated silicon and titanium isotopic compositions of presolar SiC grains from the Murchison CM2 chondrite. *Geochim. Cosmochim. Acta* **221**, 145–161.
Hans U., Kleine T. and Bourdon B. (2013) Rb-Sr chronology of volatile depletion in differentiated pro-toplanets: BABI, ADOR and ALL revisited. *Earth Planet. Sci. Lett.* **374**, 204–214.
Heydegger H. R., Foster J. J. and Compston W. (1979) Evidence of a new isotopic anomaly from titanium isotopic ratios in meteoric materials. *Nature* **278**, 704–707.
Heydegger H. R., Foster J. J. and Compston W. (1982) Terrestrial, meteoritic, and lunar titanium isotopic ratios revaluated - Evidence for correlated variations. *Earth Planet. Sci. Lett.* **58**, 406–418.
Huang S., Farkavs J., Yu G., Petaev M. I. and Jacobsen S. B. (2012) Calcium isotopic ratios and rare earth element abundances in refractory inclusions from the Allende CV3 chondrite. *Geochim. Cosmochim. Acta* **77**, 252–265.
Ireland T. R. (1988) Correlated morphological, chemical, and isotopic characteristics of hibonites from the Murchison carbonaceous chondrite. *Geochim. Cosmochim. Acta* **52**, 2827–2839.
Jarosewich E., Clarke R. S. and Barrows J. N. (1987) The allende meteorite reference sample. *Smithson. Contrib. Earth Sci.* **27**, 49.
Jochum K. P., Weis U., Schwager B., Stoll B., Wilson S. A., Haug G. H., Andreae M. O. and Enzweiler J. (2015) Reference values following ISO guidelines for frequently requested rock reference materials. *Geostand. Geoanal. Res.* **40**, 333–350.
Kleine T., Mezger K., Münker C., Palme H. and Bischoff A. (2004) ^{182}Hf-^{182}W isotope systematics of chondrites, eucrites, and Martian meteorites: Chronology of core formation and mantle differentiation in Vesta and Mars. *Geochim. Cosmochim. Acta* **68**, 2935–2946.
Kööp L., Davis A. M., Nakashima D., Park C., Krot A. N., Nagashima K., Tenner T. J., Heck P. R. and Kita N. T. (2016) A link between oxygen, calcium and titanium isotopes in 26Al-poor hibonite-rich CAIs from Murchison and implications for the heterogeneity of dust reservoirs in the solar nebula. *Geochim. Cosmochim. Acta* **189**, 70–95.
Kööp L., Nakashima D., Heck P. R., Kita N. T., Tenner T. J., Krot A. N., Nagashima K., Park C. and Davis A. M. (2018) A multielement isotopic study of refractory FUN and F CAIs: Mass-dependent and mass-independent isotope effects. *Geochim. Cosmochim. Acta* **221**, 296–317.
Kruijer T. S., Burkhardt C., Budde G. and Kleine T. (2017) Age of Jupiter inferred from the distinct genetics and formation times of meteorites. *Proc. Natl. Acad. Sci.* **114**, 6712–6716.
Langmuir C. H., Vocke R. D., Hanson G. N. and Hart S. R. (1978) A general mixing equation with applications to Icelandic basalts. *Earth Planet. Sci. Lett.* **37**, 380–392.
Levison H. F., Duncan M. J., Brasser R. and Kaufmann D. E. (2010) Capture of the Sun's Oort cloud from stars in its birth cluster. *Science* **329**, 187–190.
Leya I., Schönbächler M., Krahenbuhl U. and Halliday A. N. (2009) New titanium isotope data for Allende and Efremovka CAIs. *Astrophys. J.* **702**, 1118–1126.
Leya I., Schönbächler M., Wiechert U., Krahenbuhl U. and Halliday A. N. (2008) Titanium isotopes and the radial heterogeneity of the solar system. *Earth Planet. Sci. Lett.* **266**, 233–244.
Lin Y., Amari S. and Pravdivtseva O. (2002) Presolar grains from the Qingzhen (EH3) meteorite. *Astrophys. J.* **575**, 257–263.
Lock S. J., Stewart S. T., Petaev M. I., Leinhardt Z., Mace M. T., Jacobsen S. B. and Cuk M. (2018) The origin of the Moon within a terrestrial synestia. *J. Geophys. Res. Planets* **123**, 910–951.
Lodders K., Palme H. and Gail H. P. (2009) Abundances of the elements in the solar system. In *Landolt-Börnstein, New Series*, Vol. VI/4B (ed. J. E. Trümper). Springer-Verlag, Berlin, Heidelberg, New York, pp. 560–630 (Chap. 4.4).
Mason B. and Martin P. (1977) Geochemical differences among components of the Allende meteorite. *Smithson. Contrib. Earth Sci.* **19**, 84–95.
McKeegan K. D., Kallio A. P. A., Heber V. S., Jarzebinski G., Mao P. H., Coath C. D., Kunihiro T., Wiens R. C., Nordholt J. E., Moses R. W., Reisenfeld D. B., Jurewicz A. J. G. and Burnett D. S. (2011) The oxygen isotopic composition of the sun inferred from captured solar wind. *Science* **332**, 1528–1532.
Moynier F., Day J., Okui W., Yokoyama T., Bouvier A., Walker R. and Podosek F. A. (2012) Planetary-scale strontium isotopic heterogeneity and the age of volatile depletion of early solar system materials. *Astrophys. J.* **758**, 45.
Myojo K., Yokoyama T., Okabayashi S., Wakaki S., Sugiura N. and Iwamori H. (2018) The origin and evolution of nucleosynthetic Sr isotope variability in calcium and aluminum-rich refractory inclusions. *Astrophys. J.* **853**, 48.
Nanne J. A., Nimmo F., Cuzzi J. N. and Kleine T. (2019) Origin of the non-carbonaceous-carbonaceous meteorite dichotomy. *Earth Planet. Sci. Lett.* **511**, 44–54.
Nicolussi G. K., Pellin M. J., Lewis R. S., Davis A. M., Clayton R. N. and Amari S. (1998) Strontium isotopic composition in individual circumstellar silicon carbide grains: a record of s-process nucleosynthesis. *Phys. Rev. Lett.* **81**, 3583–3586.
Niederer F. R., Papanastassiou D. A. and Wasserburg G. J. (1980) Endemic isotopic anomalies in titanium. *Astrophys. J. Lett.* **240**, L73–L77.
Niederer F., Papanastassiou D. and Wasserburg G. J. (1985) Absolute isotopic abundances of Ti in meteorites. *Geochim. Cosmochim. Acta* **49**, 835–851.
Niemeyer S. and Lugmair G. W. (1984) Titanium isotopic anomalies in meteorites. *Geochim. Cosmochim. Acta* **48**, 1401–1416.
Niemeyer S. (1988) Isotopic diversity of nebular dust - the distribution of Ti isotopic anomalies in carbonaceous chondrites. *Geochim. Cosmochim. Acta* **52**, 2941–2954.
Nittler L. R., Alexander C. M. O., Gallino R., Hoppe P., Nguyen A. N., Stadermann F. J. and Zinner E. K. (2008) Aluminum-, calcium- and titanium-rich oxide stardust in ordinary chondrite meteorites. *Astrophys. J.* **682**, 1450–1478.
Pahlevan K. and Stevenson D. J. (2007) Equilibration in the aftermath of the lunar-forming giant impact. *Earth Planet. Sci. Lett.* **262**, 438–449.
Papanastassiou D. A. and Wasserburg G. J. (1978) Strontium isotopic anomalies in the Allende meteorite. *Geophys. Res. Lett.* **5**, 595–598.
Papanastassiou D. A., Chen J. H. and Dauphas N. (2010) Anomalous ^{53}Cr and ^{54}Cr and nearly normal Ni in differential dissolution steps of murchison. In *Lunar and Planetary Science Conference*, vol. 41, p. 2068. Lunar and Planetary Science Conference.
Patchett P. J. and Tatsumoto M. (1980) A Routine high-precision method for Lu-Hf isotope geochemistry and chronology. *Contrib. Miner. Petrol.* **75**, 263–267.
Paton C., Schiller M. and Bizzarro M. (2013) Identification of an ^{84}Sr-depleted carrier in primitive meteorites and implications

for thermal processing in the solar protoplanetary disk. *Astrophys. J. Lett.* **763**, L40.
Pignatale F. C., Charnoz S., Chaussidon M. and Jacquet E. (2018) Making the planetary material diversity during the early assembling of the solar system. *The Astrophys. J. Lett.* **867**, L23.
Pignatale F. C., Gonzalez J.-F., Cuello N., Bourdon B. and Fitoussi C. (2017) Size and density sorting of dust grains in SPH simulations of protoplanetary discs. *Monthly Notices Roy. Astron. Soc.* **469**, 237–254.
Podosek F. A., Prombo C. A., Amari S. and Lewis R. S. (2004) s-process Sr isotopic compositions in presolar SiC from the Murchison meteorite. *Astrophys. J.* **605**, 960–965.
Poole G. M., Rehkämper M., Coles B. J., Goldberg T. and Smith C. L. (2017) Nucleosynthetic molybdenum isotope anomalies in iron meteorites – new evidence for thermal processing of solar nebula material. *Earth Planet. Sci. Lett.* **473**, 215–226.
Qin L. P., Carlson R. W. and Alexander C. M. O. (2011) Correlated nucleosynthetic isotopic variability in Cr, Sr, Ba, Sm, Nd and Hf in Murchison and QUE 97008. *Geochim. Cosmochim. Acta* **75**, 7806–7828.
Regelous M., Elliott T. and Coath C. D. (2008) Nickel isotope heterogeneity in the early solar system. *Earth Planet. Sci. Lett.* **272**, 330–338.
Reisberg L., Dauphas N., Luguet A., Pearson D. G., Gallino R. and Zimmermann C. (2009) Nucleosynthetic osmium isotope anomalies in acid leachates of the Murchison meteorite. *Earth Planet. Sci. Lett.* **277**, 334–344.
Render J., Ebert S., Burkhardt C., Kleine T. and Brennecka G. A. (2019) Titanium isotopic evidence for a shard genetic heritage of refractory inclusions from different carbonaceous chondrites. *LGeochim. Cosmochim. Acta* **2245**, 40–53.
Render J., Fischer-Gödde M., Burkhardt C. and Kleine T. (2017) The cosmic molybdenum-neodymium isotope correlation and the building material of the Earth. *Geochem. Perspect. Lett.* **3**, 170–178.
Riciputi L. R., McSween H. Y. J., Johnson C. A. and Prinz M. (1994) Minor and trace element concentrations in carbonates of carbonaceous chondrites, and implications for the compositions of coexisting fluids. *Geochim. Cosmochim. Acta* **58**, 1343–1351.
Schiller M., Bizzarro M. and Fernandes V. A. (2018) Isotopic evolution of the protoplanetary disk and the building blocks of Earth and the Moon. *Nature* **555**, 507–510.
Schiller M., Paton C. and Bizzarro M. (2015) Evidence for nucleosynthetic enrichment of the protosolar molecular cloud core by multiple supernova events. *Geochim. Cosmochim. Acta* **149**, 88–102.
Schönbächler M., Rehkämper M., Fehr M. A., Halliday A. N., Hattendorf B. and Günther D. (2005) Nucleosynthetic zirconium isotope anomalies in acid leachates of carbonaceous chondrites. *Geochim. Cosmochim. Acta* **69**, 5113–5122.
Scott, E. R. D. and Krot, A. N. (2014) Chondrites and their components. In Meteorites and Cosmochemical Processes, (ed. A. M. Davis), Treatise on Geochemistry, vol. 1, 2nd ed., Elsevier. pp. 181–231
Shollenberger Q. R., Borg L. E., Render J., Ebert S., Bischoff A., Russell S. S. and Brennecka G. A. (2018) Isotopic coherence of refractory inclusions from CV and CK meteorites: Evidence from multiple isotope systems. *Geochim. Cosmochim. Acta* **228**, 62–80.
Sprung P., Scherer E. E., Upadhyay D., Leya I. and Mezger K. (2010) Non-nucleosynthetic heterogeneity in non-radiogenic stable Hf isotopes: Implications for early solar system chronology. *Earth Planet. Sci. Lett.* **295**, 1–11.
Steele R. C. J. and Boehnke P. (2015) Titanium isotope source relations and the extent of mixing in the proto-solar nebula examined by independent component analysis. *Astrophys. J.* **802**, 80.
Stracke A., Palme H., Gellissen M., Munker C., Kleine T., Birbaum K., Gunther D., Bourdon B. and Zipfel J. (2012) Refractory element fractionation in the Allende meteorite: Implications for solar nebula condensation and the chondritic composition of planetary bodies. *Geochim. Cosmochim. Acta* **85**, 114–141.
Travaglio C., Gallino R., Arnone E., Cowan J., Jordan F. and Sneden C. (2004) Galactic evolution of Sr, Y, And Zr: A multiplicity of nucleosynthetic processes. *Astrophys. J.* **601**, 864–884.
Trinquier A., Birck J.-L. and Allegre C. J. (2007) Widespread ^{54}Cr heterogeneity in the inner solar system. *Astrophys. J* **655**, 1179.
Trinquier A., Elliott T., Ulfbeck D., Coath C., Krot A. N. and Bizzarro M. (2009) Origin of nucleosynthetic isotope heterogeneity in the solar protoplanetary disk. *Science* **324**, 374–376.
Van Kooten E. M. M. E., Wielandt D., Schiller M., Nagashima K., Thomen A., Larsen K. K., Olsen M. B., Nordlund Å., Krot A. N. and Bizzarro M. (2016) Isotopic evidence for primordial molecular cloud material in metal-rich carbonaceous chondrites. *Proc. Nat. Acad. Sci. USA* **113**, 2011–2016.
Visser R., van Dishoeck E. F., Doty S. D. and Dullemond C. P. (2009) The chemical history of molecules in circumstellar disks. *Astron. & Astrophys.* **495**, 881–897.
Walker R. J. (2012) Evidence for homogeneous distribution of osmium in the protosolar nebula. *Earth Planet. Sci. Lett.* **351–352**, 36–44.
Warren P. H. (2011) Stable-isotopic anomalies and the accretionary assemblage of the Earth and Mars: A subordinate role for carbonaceous chondrites. *Earth Planet. Sci. Lett.* **311**, 93–100.
Wasserburg G. J., Trippella O. and Busso M. (2015) Isotope Anomalies in the Fe-group Elements in Meteorites and Connections to Nucleosynthesis in AGB Stars. *Astrophys. J.* **805**, 7.
Wasson J. T. and Kallemeyn G. W. (1988) Compositions of chondrites. *Philosoph. Trans. Roy. Soc. London Ser. A-Math. Phys. Eng. Sci.* **325**, 535–544.
Williams C., Janney P., Hines R. and Wadhwa M. (2016) Precise titanium isotope compositions of refractory inclusions in the Allende CV3 chondrite by LA-MC-ICPMS. *Chem. Geol.* **436**, 1–10.
Woosley S. E. and Heger A. (2007) Nucleosynthesis and remnants in massive stars of solar metallicity. *Phys. Rep.* **442**, 269–283.
Worsham E. A., Bermingham K. R. and Walker R. J. (2017) Characterizing cosmochemical materials with genetic affinities to the Earth: Genetic and chronological diversity within the IAB iron meteorite complex. *Earth Planet. Sci. Lett.* **467**, 157–166.
Worsham E. A., Burkhardt C., Budde G., Fischer-Gödde M., Kruijer T. S. and Kleine T. (2019) Distinct evolution of the carbonaceous and non-carbonaceous reservoirs: Insights from Ru, Mo, and W isotopes. *Earth and Planetary Science Letters* **521**, 103–112.
Yang L. and Ciesla F. J. (2012) The effects of disk building on the distributions of refractory materials in the solar nebula. *Meteorit. Planet. Sci.* **47**, 99–119.
Yokoyama T., Alexander C. M. O'D. and Walker R. J. (2010) Osmium isotope anomalies in chondrites: Results for acid residues and related leachates. *Earth Planet. Sci. Lett.* **291**, 48–59.
Yokoyama T., Fukami Y., Okui W., Ito N. and Yamazaki H. (2015) Nucleosynthetic strontium isotope anomalies in carbonaceous chondrites. *Earth Planet. Sci. Lett.* **416**, 46–55.

Yokoyama T., Rai V. K., Alexander C. M. O'D., Lewis R. S., Carlson R. W., Shirey S. B., ThiernenS M. H. and Walker R. J. (2007) Osmium isotope evidence for uniform distribution of s- and r-process components in the early solar system. *Earth Planet. Sci. Lett.* **259**, 567–580.

Zhang J. J., Dauphas N., Davis A. M., Leya I. and Fedkin A. (2012) The proto-Earth as a significant source of lunar material. *Nat. Geosci.* **5**, 251–255.

Zhang J. J., Dauphas N., Davis A. M. and Pourmand A. (2011) A new method for MC-ICPMS measurement of titanium isotopic composition: identification of correlated isotope anomalies in meteorites. *J. Anal. At. Spectrom.* **26**, 2197–2205.

Zinner, E. (2014) Presolar grains. In Meteorites and Cosmochemical Processes (ed. A. M. Davis), Treatise on Geochemistry, vol. 1, 2nd ed., Elsevier. pp. 181–231.

Associate editor: Anders Meibom